

Review of indirect detection methods of dark matter

GRAPPA Student Seminar

by Paul Hoffland, Bouke Jung and Iris de Ruiter

June 2018

Abstract

In this review we will discuss various methods to indirectly detect dark matter. Where direct detection experiments look for the scattering of a dark matter particle of nucleus or electron, indirect detection methods look for products of the annihilation of two dark matter particles. Products that we search for include gamma-rays, CMB photons, positrons, antiprotons and anti-nuclei. There have not been actual detections of the annihilation of dark matter. This lack of observations gives rise to strong constraints on the dark matter parameters space, i.e. the dark matter mass and annihilation cross section (m_χ and $\langle \sigma v \rangle$). In this review we will consider the gamma-ray, CMB and anti-matter indirect detection channels. We'll discuss the theoretical framework for each of these methods, the observational results and make predictions for the future.



UNIVERSITEIT VAN AMSTERDAM

GRAPPA

GRavitation AstroParticle
Physics Amsterdam



Source code, scripts and presentations can be found at:
https://github.com/bradkav/GSS2018_Indirect

Contents

1	Introduction - (Iris & Bouke)	3
2	Gamma-ray experiments	6
2.1	Gamma-ray flux from dark matter WIMP annihilation - (Paul)	6
2.1.1	Particle physics factor	6
2.1.2	Astrophysical factor	7
2.1.3	Sagittarius gamma-ray flux	9
2.2	Probing Dark Matter Distributions - (Bouke)	9
2.2.1	Translating observational data to dark matter densities	10
2.2.2	Dark matter distribution profiles	11
2.3	Current and future gamma-ray telescopes and their constraints on the dark matter cross section - (Iris)	13
2.3.1	Fermi-LAT	14
2.3.2	H.E.S.S.	14
2.3.3	VERITAS, MAGIC and HAWC	15
2.3.4	Future telescopes	15
2.3.5	Comparison of gamma-ray telescopes	16
2.4	Smoking gun for the detection of dark matter annihilation - (Iris)	17
3	CMB constraints on dark matter	18
3.1	Cosmological history with the CMB power spectrum - (Iris)	18
3.2	Dark matter annihilation at recombination - (Iris)	19
3.3	Sommerfeld enhancement - (Iris)	20
3.4	Cosmological signatures of dark matter self-annihilation - (Bouke)	21
3.4.1	Methodology	21
3.5	Observational constraints of self-annihilation cross section from WMAP and PLANCK data - (Paul)	26
3.5.1	WMAP	27
3.5.2	Planck	28
4	Dark matter detection with anti-matter	30
4.1	The Positron channel - (Bouke)	30
4.1.1	Expectations for the positron fraction and the electron + positron flux	30
4.1.2	Dark Matter annihilation	32
4.1.3	Other potential sources: pulsars and pulsar wind nebulae	33
4.2	Antiproton channel - (Iris)	36
4.2.1	Astrophysical antiproton background	36
4.2.2	Antiproton dark matter constraints	37
4.3	Anti-nucleus channel - (Paul)	39
4.3.1	Anti-nuclei production	39
4.3.2	Coalescence momentum p_0	40
4.3.3	Propagation through the galactic medium	41
4.3.4	Propagation through the heliosphere	42
4.3.5	Flux predictions	42
5	Summary - (Iris & Paul)	44
6	Appendix	46
6.1	Appendix A: Lunar assisted trajectory	46
6.2	Appendix B: Jupyter notebook	46

1 Introduction - (Iris & Bouke)

One of the most important endeavours in contemporary astrophysics is to understand the nature of dark matter in the Universe. The long-held paradigm is that dark matter is non-baryonic and cold (non-relativistic) and is made up of some Weakly Interacting Massive Particles (WIMPS). The fact that we believe dark matter is cold implies that there is a relic dark matter density from decoupling (freeze-out) of the thermal plasma in the early Universe. The most popular WIMP candidate still remains the neutralino, as predicted by the supersymmetric extension of the standard model (SUSY). For more information on the dark matter candidates see the review article about candidates on this website. Dark matter candidates are often predicted in the GeV-TeV energy range and can be detected with two distinct methods; Direct and Indirect. Note that no real dark matter signal has been detected so far (for claims of a detection see for example [1] and [2]), but certain candidates have been either constrained or excluded [3]. Despite the fact that dark matter has not been detected, indirect cosmological phenomena tell us that there must exist something like dark matter. Compelling pieces of evidence for a dark matter particle are given in the rotation curves of galaxies, the collision of the Bullet cluster and gravitational lensing. For more information on this subject see the review about dark matter and cosmology on this website.

There are different ways to look for dark matter. Direct measurement methods look for interactions between WIMPS and ordinary baryonic particles (such as *Ge*, *NaI*, *Xe*, *CaF₂* molecules [4]). For more information on the direct detection of dark matter see the review article about direct detection on this website. The indirect methods look for either gamma-rays, positrons, antiprotons or other products from dark matter self-annihilation. These particles are produced indirectly by pairs of WIMPs that annihilate into either quarks or leptons. Although direct $\gamma\gamma$ or $Z\gamma$ annihilation lines are in theory possible, they are loop-suppressed. Therefore, the most interesting annihilation channels are those of pairs of quarks or leptons that will further decay into gamma-rays (via for example pions), positrons and antiprotons. Uncertainty in the astrophysical background can however create issues for the latter method. To be able to distinguish for example gamma-rays from dark matter annihilation from the astrophysical background, we have to precisely know the astrophysical gamma-ray background. In this review we will discuss various methods to indirectly detect dark matter. All detection methods look for products of the annihilation of two dark matter particles.

Before explaining any of the indirect dark matter detection methods in detail, it is important that we properly discuss signals that may arise from dark matter annihilation. Although no signal has been observed as of yet — at least not unambiguously — it is possible to derive stringent theoretical limits on the various resulting particle spectra one might expect.

Let us start by analyzing what may prospect a dark matter WIMP to behave like. In order for a WIMP to be able to undergo self-annihilation, the particle would have to constitute either a Majorana fermion (i.e. a fermionic particle that is its own antiparticle) or a Dirac fermion. In the latter case, it would be quintessential that there is no matter-antimatter asymmetry from an observational point of view, since no dark matter antiparticle annihilation partners would remain for us to observe a signal otherwise. Further constraints on the dark matter WIMP nature are given by cosmological considerations. In chapter 3 we'll see that our current knowledge of CMB angular power spectra sets stringent upper limits on dark matter annihilation rates, depending upon mass of the particle under consideration (i.e. $\langle\sigma v\rangle < 10^{-25}\text{cm}^3\text{s}^{-1}$ for a WIMP mass of a few hundred GeV). As a consequence of the low dark matter cross section, that corresponds with this, local dark matter densities will have to be quite high in order for us to observe any annihilation signal at an appreciable level. Important to keep in mind is that the width of the annihilation process will depend quadratically on the number density of dark matter particles ($\Gamma \propto n^2 \propto \rho^2$), since a particle and antiparticle (i.e. 2 particles in total) will have to meet before annihilation can actually occur.

The rate at which WIMP particle-antiparticle rendezvous take place, depends on a number of parameters. One of them is the average relative velocity between the WIMPs. In most regions, this is assumed to be close to zero, resulting in the so-called *S-wave approximation*. Particles produced as an effect of an S-wave annihilation process $\chi + \chi \rightarrow A + B$ are constrained in their energy-budget in the sense that $2m_\chi \geq m_A + m_B$. Hence, to leading order the particle products will consist mostly of standard model fermions/anti-fermions and neutral pair combinations of gauge or Higgs bosons of all types. In the interstellar medium (ISM) the various particles which were created from dark matter annihilation may undergo further interactions, such as decays and hadronizations, eventually giving rise to the final state particles we observe on Earth.

An important aspect of indirect detection methods are the various particle annihilation channels which are expected for supersymmetric (SUSY) WIMP models¹. To discuss these annihilation channels, let us summarize a discussion presented in Carr et al. (2006) [5]. Annihilation products within SUSY models depend heavily on the higgsino and gaugino content of the neutralino mixed particle state. Since only the higgsino and wino parts of a neutralino couple to the minimal supersymmetric standard model (MSSM) gauge bosons, no type of neutralino except those that are wino- or higgsinolike will decay into massive gauge bosons or Higgs bosons (i.e. pairs such as $Z^0 Z^0$, $W^+ W^-$, $Z^0 h(H)$, $Z^0 A$, $W^{+/-} H^{-/+}$, $H^+ H^-$ and combinations of A , h and H). Hence, on the tree level, decay into MSSM bosons will mostly occur via neutralino/chargino exchanges in t-channel interactions or s-channel interactions involving $Z^0/A/h/H$ particles.

In the S-wave approximation, where the neutralino's are assumed to display near-zero relative motion, several decay mechanisms will be suppressed as a consequence of the Pauli exclusion principle². Furthermore, helicity suppression arising from the non-contribution of the Z^0 boson transverse part, will severely restrict the creation of low mass and massless fermion-antifermion pairs. As a consequence, pair creation of massive fermions is favoured. Moreover, since down-type quarks are enhanced by a factor $\tan \beta$, whilst up-type quarks are suppressed by a factor $1/\tan \beta$ (where β denotes the CKM matrix angle), bottom type quarks will dominate the final particle spectrum. This means that $b\bar{b}$ -pairs form the most likely products of neutralino WIMP annihilation, followed by lepton pairs and massive gauge bosons, depending upon the neutralino WIMP mass. Note, however, that the primary annihilation products are not directly the ones we observe on Earth. Potential detections of gamma-rays and cosmic-rays that might be associated with dark matter annihilation, are thought to derive from a cascade of intermediate decays and hadronizations instead. For example, with regards to the dark matter annihilation origin of gamma-rays, it is believed that the initial ($b\bar{b}$) particle-antiparticle pairs go on to form neutral pions, which subsequently decay either directly into two gamma-rays or into electron-positron pairs that undergo thermal Bremsstrahlung. For a more detailed discussion of the various final particle spectra and constituent annihilation channels, see chapter 4 of the paper by Gaskins, published in 2016 [6].

Something which inhibits our ability to make predictions for indirect detection from injected cosmic ray spectra, is the potential occurrence of diffusive processes while particles propagate through the interstellar medium. As we will see in the following chapter, such processes will not affect gamma-rays in any dramatic way. However, charged cosmic rays are likely to dissipate energy under the influence of magnetic turbulence. As a consequence, it is necessary to keep diffusion in mind, when considering the dark matter induced cosmic-ray spectra observable on Earth. We will see in chapter 4 that several astrophysical sources might be able to mimic cosmic-ray spectra which we expect from dark matter annihilation.

¹For an overview of the general theory surrounding SUSY models, see the review of dark matter particle candidates on this website.

²The particles comprising an annihilating neutralino particle-antiparticle pair with zero relative motion, must have opposite spin. This causes the CP-odd initial state and the null total angular momentum to be conserved, which in turn results in the suppression of several annihilation channels. See Carr et al. (2006) [5] and references therein for a more thorough discussion.

In relation to the final state energy spectra of dark matter annihilation processes, we should stipulate one signature which could be considered a 'smoking gun' for dark matter indirect detection. This would be a unique spectral line in the gamma-ray (or charged lepton cosmic ray) spectrum, which are directly related to the neutralino WIMP mass. Unfortunately, such gamma-ray lines are loop suppressed in most dark matter models. For example, in the case of the SUSY WIMP model discussed in the section above a distinct spectral line could be created via the box process $\chi\chi \rightarrow \gamma\gamma, \gamma Z^0$, with an energy $E_\gamma = m_\chi$ or, respectively, $E_\gamma = (4m_\chi^2 - m_Z^2)/4m_\chi$. Contrarily, annihilation processes involving the generation of quark-antiquark (e.g. $b\bar{b}$) pairs will always result in continuum spectra for gamma-rays, as a consequence of the preceding cascade of decays and hadronizations. In this case, the best way to model resulting spectra, is to use either numerical Monte Carlo simulations [7, 8] or parametrized fragmentation functions with simple phase space arguments [9, 10]. Both methods generally yield simple spectral dependencies on the WIMP mass.

In this review we'll discuss the signal from products of dark matter annihilation. Products that we discuss include gamma-rays, CMB photons, positrons, antiprotons and anti-nuclei. For the gamma-rays we describe the theoretical flux that we expect from dark matter annihilation, different dark matter density distributions and current and future constraints by a variety of gamma-ray telescopes. For the CMB constraints we'll again discuss the theoretical impact of dark matter annihilation on recombination in the early Universe. After that we'll discuss how this relates to the CMB power spectrum and the constraints as set by WMAP and Planck. Finally for the anti-matter channels, we'll go into the positron, antiproton and anti-nucleus channels and constraints.

2 Gamma-ray experiments

One of the ways to indirectly detect dark matter particles is to look for the gamma-ray signature of their annihilation. Two dark matter particles can annihilate to two standard model particles which then decay and leave a distinct signature in gamma-rays. The exact way this leads to gamma-ray emission is explained in the introduction, but is given in summary below. The bottom quarks produced in dark matter annihilation undergo hadronization from which a neutral pion is produced that then decays into gamma-rays. The tau leptons follow the same path to produce gamma-rays or emit gamma-rays via bremsstrahlung. The bottom quarks and tau channel are the main channels for gamma-ray experiments.

Via these paths we are able to link gamma-rays to dark matter annihilation. Using gamma-ray telescopes that point to different regions of the sky with different optimal energy ranges, we can probe the dark matter content within the local Universe. Gamma-rays are extremely powerful in creating a dark matter density map of the Universe since they are not deflected by magnetic fields, contrary to e.g. cosmic rays. There are however a lot of background gamma-rays sources that "contaminate" the interesting dark matter contribution.

In section 2.1 we will discuss how the expected gamma-ray flux depends on the dark matter cross section and mass. Comparing the corresponding formulae to observations, it is possible to set an upper limit to the dark matter mass and cross section by the absence of an annihilation signal. In section 2.2 different complications in translating observation data to actual dark matter densities are discussed. Furthermore some typical examples of dark matter density profiles are explained. Finally in section 2.3 the current and future gamma-ray telescopes, and their efforts on constraining the dark matter parameters, are discussed.

2.1 Gamma-ray flux from dark matter WIMP annihilation - (Paul)

As said before, we will consider neutral WIMPs that only interact through gravitational force and annihilate into Standard Model particles via the weak interaction. Gamma rays are one of the decay products of this annihilation. The energy and angle dependent gamma-ray brightness for this annihilation process is given by formula 1:

$$I_\gamma(E, \Theta) = \frac{1}{2} \frac{\langle \sigma v \rangle}{m_{DM}^2} \frac{dN_{\gamma, ann}}{dE_\gamma} \frac{1}{4\pi} \int dl \rho_{DM}^2(r[l, \Theta]) \quad (1)$$

where the first half of equation 1 depends on the particle physics model of dark matter (i.e. particle physics) and the second half on the dark matter distribution (i.e. astrophysics). First, an explanation of the particle physics factor will follow, after which the astrophysical factor will be discussed.

2.1.1 Particle physics factor

The velocity-averaged dark matter pair annihilation cross section $\langle \sigma v \rangle$ can be estimated by considering the observed cosmological relic abundance due to freeze-out and linking this to the pair annihilation rate of dark matter (i.e. $n \cdot \langle \sigma v \rangle \sim H$ at thermal equilibrium). Since $\Omega h^2 \sim 0.1$ [11] is the best fitted parameter to current CMB data, this implies a thermal relic cross section $\langle \sigma v \rangle \sim 3 \times 10^{-26} \text{cm}^3 \text{s}^{-1}$, see formula 2. A detailed explanation can be found in [12]. For which T_0 and H_0 are the temperature and Hubble rate today, and H the Hubble rate at freeze-out. Lastly, m_{DM} denotes the WIMP mass, $x_{f0} \equiv m_{DM}/T$ at freeze out and ρ_c the critical density.

$$\Omega_{DM} h^2 = \frac{x_{f0}}{m_{DM}^2 \langle \sigma v \rangle} \frac{T_0^3 h^2 H}{30 \rho_c} \sim \frac{3 \times 10^{-27} \text{cm}^3 \text{s}^{-1}}{\langle \sigma v \rangle} \quad (2)$$

The differential spectrum of emitted gamma-rays per annihilation, $\frac{dN_{\gamma,ann}}{dE_{\gamma}}$, can be seen as the sum (weighted by branching ratio, see formula 3) of all spectra final states, see figure 1. Since the branching ratio and final states are very model dependent, there are major uncertainties involved in trying to explain all observable dark matter using a single WIMP dark matter candidate. The differential spectrum is given by:

$$\frac{dN_{\gamma,ann}}{dE_{\gamma}} = \sum_i B_i \frac{dN_{\gamma,ann}^i}{dE_{\gamma}} \quad (3)$$

where B_i is the model depended branching ratio, and $\frac{dN_{\gamma,ann}^i}{dE_{\gamma}}$ the individual final state spectra. The gamma-ray brightness also contains a factor $\frac{1}{2}$, which implies that dark matter is its own anti-particle, this would be a factor $\frac{1}{4}$ otherwise. And lastly dividing by m_{DM}^2 cancels out the density squared integral from the astrophysical factor, since cosmological constraints can be put on the density ρ instead of the number density n of a dark matter halo. Furthermore, figure 1 shows a simulated gamma-ray spectrum for six different channels due to dark matter annihilation. A clear separation is notable between the so called hard states (i.e. e^+e^- , $\mu^+\mu^-$ and $\tau^+\tau^-$ channels) and soft states (i.e. $b\bar{b}$, $t\bar{t}$ and W^+W^- channels). In which the hard states produce gamma-rays primarily through Bremsstrahlung (dashed lines), and the soft states through pion decay (solid lines).

With the exception of the $\tau^+\tau^-$ channel, which also creates photons through pion decay (see blue dashed line) causing a higher spectrum then other hard states. The broad nature of these spectra makes it easier to be detected, although introducing uncertainties because of less understood aspects of propagation.

2.1.2 Astrophysical factor

The second half of the gamma-ray brightness (formula 1), consist only of the so called J-factor, which describes the amount and distribution of dark matter in a particular source. More exact; it is the line of sight integral over the dark matter density squared (ρ_{DM}^2) at an angle from the line of sight, see formula 4 for its definition.

$$J = \frac{1}{\Delta\Omega} \int \int_{\Delta\Omega} \rho_{DM}^2(l, \Omega) dl d\Omega \quad (4)$$

Note that in formula 1, the factor $\frac{1}{4\pi}$ is a normalization factor that comes from integrating over solid angle. Figure 2 shows our own simulations of the J-factor for different galaxies as a function of angular separation with the line of sight. As you would expect, further away galaxies will result in a lower J-factor. The J-factor found in the literature agree more or less with the derived ones. However, some discrepancies are visible for the dwarf galaxy Carina, which probably come from uncertainties in the scale density and radius that are used. The error bars refer to 1σ significance, taken from [14] where the error bars are estimated due to large uncertainties in the cosmological parameters.

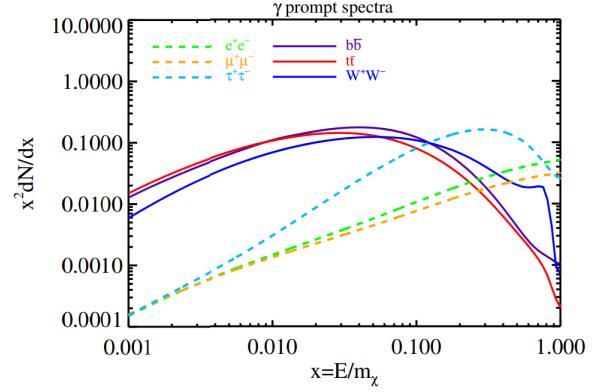


Figure 1: Figure from [6]: Gamma-ray spectrum from dark matter ($m_{DM} = 500 GeV$) annihilation to six different final states, calculated using PPPC4DMID [13]

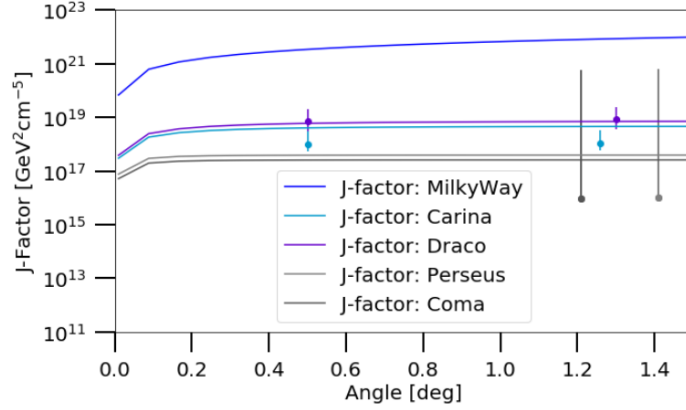


Figure 2: J-factor simulation for several dwarf galaxies and galaxy clusters, parameters from [15, 14, 16].

The dark matter density functions (ρ_{DM}) are dependent on the physical situations and only depend on the radial distance to the center of the dark matter source, r . This will be explained in greater detail in chapter 2.3. To compute the line of sight integral, we first need to relate R to L and Θ (see figure 3).

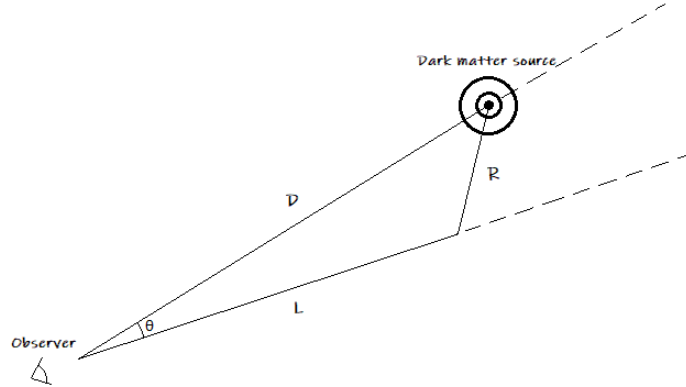


Figure 3: Top down view of observer looking down the line of sight with some angular separation Θ at a dark matter source.

Using D to denote the distance to the dark matter source and writing L for the line of sight, R for shortest distance from the line of sight to the center of the source and Θ for the angular separation of the source, we can relate R to L and Θ using the cosine rule to get formula 5.

$$R = \sqrt{L^2 + D^2 - 2LD \cos \Theta} \quad (5)$$

Looking back at the total gamma-ray brightness (formula 1) and comparing this to the annihilation rate per volume (see formula 6), it becomes clear that formula 1 is just the annihilation rate per volume times the total differential spectrum of emitted gamma-rays integrated over some volume.

$$\text{Rate of annihilation per volume: } \frac{1}{2} \frac{\langle \sigma v \rangle \rho_{DM}^2}{m_{DM}^2} \quad (6)$$

2.1.3 Sagittarius gamma-ray flux

To conclude this section we show an example of a computed gamma-ray flux spectrum as a function of dark matter mass (m_χ) per annihilation channel for dwarf galaxy Sagittarius [17] (see figure 4). Dwarf galaxies are excellent objects for this dark method detection method, since there lack large astrophysical objects such as stars and therefore do not emit a lot of gamma-rays compared to active galaxies. Measuring any gamma-ray flux from these object, almost certainly hints towards dark matter.

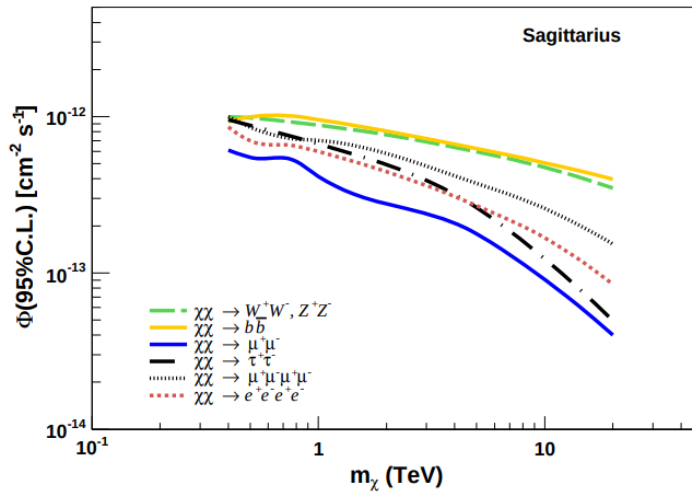


Figure 4: Figure from [17]: Gamma-ray flux simulation as a function of dark matter mass (m_χ) for different annihilation channels in the Sagittarius dwarf galaxy.

In the spectrum shown in figure 4 we find that the hard states indeed show a larger suppression for higher energies than the soft state channels. This comes from the fact that, the hard channels radiate photons at final state, the soft channels decay mainly from pions. Note that the gamma-ray flux scales with $1/m_{DM}^2$, and therefore scales down exponentially with mass, assuming some dark matter density profile. In other words; higher WIMP mass means less annihilation processes per dark matter source and therefore less gamma-rays through all channels. It should also be noted that an extreme low flux is to be expected from these dwarf galaxies i.e. $O(10^{-12})cm^2s^{-1}$. Although dwarf galaxies are ideal objects for this method, measuring low fluxes can still be very challenging. Because of this, no signal has yet to be detected with any significance.

2.2 Probing Dark Matter Distributions - (Bouke)

Having discussed the theoretical background of indirect dark matter signals, the natural question arises how these signals actually manifest in the observable Universe. A proper answer can only be provided in the context of the distribution of dark matter within the local Universe. After all, one expects to observe a brighter gamma-ray signal in regions with high dark matter density. Over the past decades great effort has been made to model and constrain the distribution of dark matter within the Milky Way and surrounding astrophysical objects. A few examples of recent findings are given by the discovery that the Milky Way does not conform to density profiles created from adiabatic compression [18] and the fact that neighbouring dwarf galaxies seem to exhibit dark matter distributions which become constant towards their galactic center [19]. Perhaps even more groundbreaking was the work of Diemand et al. (2008), who found evidence for the fact that dark matter can cluster together locally, forming complicated substructures which boost gamma-ray production by over an order of magnitude and cosmic ray production by a typical factor of 1.4 [20].

In this section we'll summarize some of the most prevalent models used in the context of indirect dark matter studies. Before explaining the various parameters and equations involved, however, we will first take another look at the relation between observed gamma-ray spectra and underlying dark matter distributions, in an attempt to form a better understanding of the difficulties involved with inferring flux rates from certain dark matter density profiles and vice versa.

2.2.1 Translating observational data to dark matter densities

The gamma-ray fluxes detected at observatories such as Fermi-LAT and the future CTA in principle contain all the information one needs in order to map dark matter distributions across galactic planes and large scale structures. As we've seen in section 2.1, there exists a direct theoretical correspondence between a source's gamma-ray intensity and the line-of-sight integral over the dark matter density. However, this is not the whole story. In making a direct comparison between the line-of-sight integral and observational fluxes, we implicitly neglect several processes of radiative transfer which could have lead to redistribution of initial dark matter generated gamma-ray fluxes — not to mention the fact that some gamma-ray detections could be misinterpreted as indirect dark matter signals, having a completely different origin all the while! Hence, in order to derive accurate conclusions regarding dark matter distributions via gamma-ray fluxes, we first have to discuss radiative transfer effects. Additionally we have to exclude the possibility of misinterpreting background signals.

Once a gamma-ray has been created through dark matter annihilation or decay, several processes might occur to it which alter the gamma-ray's energy before it reaches an observatory. Most prominent are perhaps Compton scattering and pair production. In the latter case, particle-antiparticle pairs (usually electrons and positrons) are formed out of two photons. A quick order-of-magnitude calculation reveals that if the dark-matter-induced gamma-ray would undergo such a process together with a typical 2.7 Kelvin photon of the cosmic microwave background (CMB) (i.e. $k_B \cdot T \approx 8.6 \cdot 2.7 \approx 10^{-4} \text{eV}$) whilst traveling through the interstellar medium, it would need to have an energy of at least $E_{\gamma,1} \cdot E_{\gamma,2} \approx E_{\gamma,1} \cdot 6.6 \cdot 10^{-4} \text{eV} \approx m_e^2 \approx 2.5 \cdot 10^{11} \text{eV}^2$. Hence, the photon initially created from dark matter annihilation or decay, would be required to have an energy greater than a few hundred TeV. For space-based gamma-ray observatories such as Fermi-LAT, which generally operate at energies of a few hundred MeV to several hundred GeV, this process should therefore not constitute any impairment in detecting dark-matter-induced gamma-rays. The upcoming Cherenkov Telescope Array (CTA) which is planned to operate between a few hundred GeV and a few hundred TeV, might have to take the process into account.

Compton scattering may form a problem when the produced gamma-rays travel through areas in interstellar space with high electron densities. Typically, however, induced effects will not be relevant. Taking a characteristic electron density of a few particles per cubic centimetre and assuming that the Thomson approximation holds³ we see that the optical depth associated with Compton scattering for a source at a distance of a few kpc would be:

$$\tau \approx n_e \sigma_T h d \approx 1 \text{ cm}^{-3} \cdot 1 \times 10^{-24} \text{ cm}^2 \cdot 1 \times 10^{22} \text{ cm} \approx 10^{-5}$$

Hence we can conclude that galaxies are typically very optically thin when it comes to Compton scattering. This allows one to largely ignore such processes in studying indirect dark matter signals, provided that the gamma-rays one observes did not have to propagate through any dense interstellar regions.

³To be precise one would need to input the Klein-Nishina cross section for this scattering process. However, since the Thomson cross section is always bigger, we can use $\sigma_T h$ instead to retrieve an upper limit.

2.2.2 Dark matter distribution profiles

Provided that any ambiguities in ones signal have been thoroughly discussed and ruled out, it is in principle possible to construct dark matter density profiles for astrophysical objects using formula 2.1. Usually, however, researchers take the density profile as an input parameter and try to reproduce observed emission spectra numerically for comparison purposes. Over the years, a variety of different models have come into use [6]. The most recognizable one is perhaps the *Navarro-Frenk-White* (NFW) profile:

$$\rho_{NFW} = \frac{\rho_0}{\left(\frac{r}{r_s}\right) \left[1 + \left(\frac{r}{r_s}\right)\right]^2} \quad (7)$$

where r denotes the distance from the center of the galactic halo and r_s is a scale radius, indicating the point where the logarithmic derivative of the radial density profile becomes equal to -2. In the case of the Milky Way, Fornasa and Green (2014) [21] established that $r_s \approx 20$ kpc, resulting in a dark matter density at the Sun's position of around 0.4 GeV/cm^3 .

Some slightly more involved profiles try to account for various deviations that cannot be modeled accurately by a pure NFW density profile. Particularly they create steeper profiles at the inner edges of the dark matter halo, since mechanisms involving (gravitational) interactions between dark matter and baryonic matter such as adiabatic contraction are expected to yield more concentrated dark matter distributions towards the galactic center [22, 23, 24]. Generalizing equation 2.2.2 and allowing for an arbitrary inner slope γ , we get the formula:

$$\rho_{GNFW} = \frac{\rho_0}{\left(\frac{r}{r_s}\right)^\gamma \left[1 + \left(\frac{r}{r_s}\right)\right]^{3-\gamma}} \quad (8)$$

which reverts back to equation 2.2.2 for $\gamma = 1$. Observationally, we typically find that $0 \leq \gamma \leq 1.5$, where $\gamma = 0$ corresponds to a so-called *coned* profile, whilst $\gamma = 1.5$ is also referred to as a Moore profile [25, 26].

Contrary to the above two profiles, more recent simulations seem to suggest that galactic dark matter density profiles deviate from simple power-law dependencies, displaying slopes that vary with radius instead [27, 28, 29]. One of the first attempts at modeling such irregularity was made by *Einasto* [30], who proposed the formula:

$$\rho_{Ein}(r) = \rho_0 \exp\left(-\frac{2}{a} \left[\left(\frac{r}{r_s}\right)^a - 1\right]\right) \quad (9)$$

Observations for the Milky Way yield values around 0.2 for the parameter a .

One last dark matter density profile that we'll have to discuss is called *the Burkert profile*:

$$\rho_{Burk}(r) = \frac{\rho_0}{\left(1 + \frac{r}{r_s}\right) \left(1 + \left(\frac{r}{r_s}\right)^2\right)} \quad (10)$$

This model distinguishes itself from the rest, because it quickly flattens towards the galactic core. In the context of spheroidal dwarf galaxies, this is especially relevant, since a number of different studies on rotation curves show that their density profiles becomes less steep at small radii [31, 32].

Assuming that the objects have a minimal disk and a spherical dark matter halo, the r -dependence of the halo density can be well approximated by inverting the rotation curve. This can be accomplished

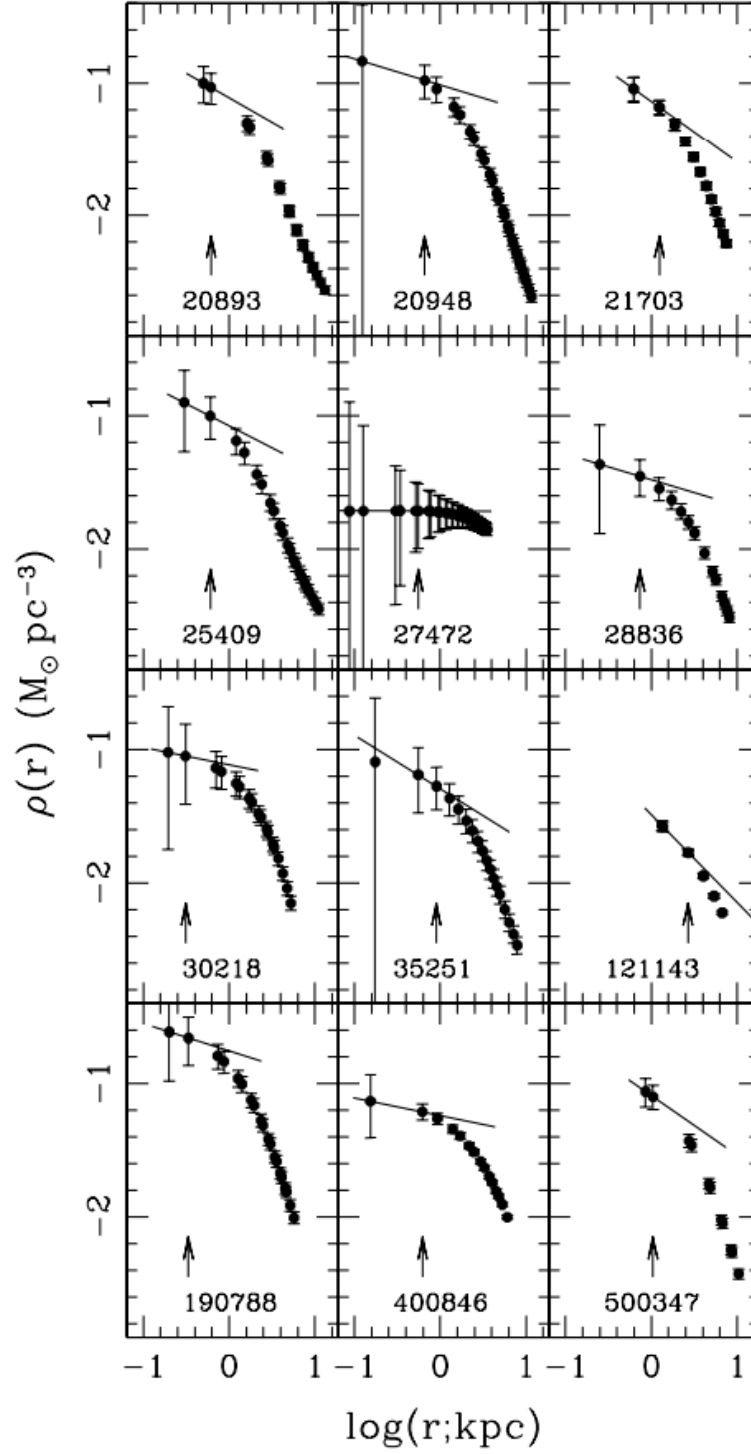


Figure 5: Density profiles of a collection of different spheroidal dwarf galaxies as derived from rotation curves in Spekkens et al. (2005) [32]. A solid, straight line indicates the linear least-squares fit used to characterize the inner halo density slope. All points above to and left from the indicated arrows were included in the respective fits.

via a direct application of Poisson's equation, yielding the expression:

$$\rho(r) = \frac{1}{4\pi G} \left[2 \frac{v(r)}{r} \frac{dv(r)}{dr} + \frac{V^2(r)}{r^2} \right] \quad (11)$$

Figure 5 shows the dark matter halo density profiles calculated using this formula for a number of different spheroidal dwarf galaxies, following the analysis of a sample of 165 rotation curves. Although it's still some matter of debate to which extent spheroidal dwarf galaxies display cusp- (i.e. steep towards the center) or core-like (i.e. constant towards the center) density profiles, the graph clearly shows that the halo densities of dwarfs flatten towards the center. Considering that spheroidal dwarf galaxies generally consist of a very low density, homogeneously distributed gas, this should come as no real surprise

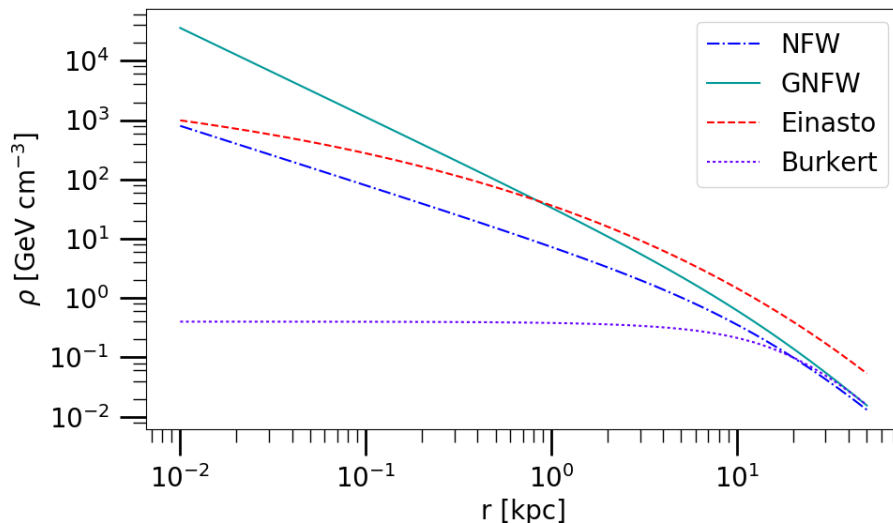


Figure 6: A graph of the various dark matter density profiles discussed within section 2.2.2. All profiles are generated using an input density $\rho_0 = 0.4$ and a scale radius $r_s = 20$ kpc. Additionally, the GNFW spectrum was given an index $\gamma = 1.5$, whilst the Einasto spectrum received an index $a = 0.2$.

Figure 6 displays the various dark matter density profiles discussed within this section in a single panel. The differences between each of the profiles is clearly visible. The GNFW profile is the steepest and leads to large densities at the galactic core. Meanwhile, the Burkert density profile quickly flattens as the radius decreases, conform our expectations for an elliptic dwarf galaxy, which generally constitute relatively low mass, and homogeneous companion galaxies to a main host.

2.3 Current and future gamma-ray telescopes and their constraints on the dark matter cross section - (Iris)

Now that we have a complete picture of the theoretical background we can take a look at some actual gamma-ray observations. As said before we hope to detect dark matter particles via their annihilation signature. Two dark matter particles can annihilate to two standard model particles which then decay and leave a distinct signature in gamma-rays. Gamma-ray telescopes focus on the detection of gamma-rays from this dark matter annihilation process. This process is usually split up into multiple channels. The most important examples are $\chi\chi \rightarrow b\bar{b}$ and $\chi\chi \rightarrow \tau^+\tau^-$, where the free quarks and leptons will further decay into gamma-rays. The constraints given on the mass and cross section for the dark matter particle are given for each of these annihilation channels (bottom quarks and

tau leptons), where the tau channel usually gives the strongest constraints. In the search for these annihilation processes most observations look directly at the dark matter halo of our Milky Way since this is one of the most dark matter dense regions (see section 2.2.1). Another approach is to look at spheroidal dwarf galaxies, which are dominated by dark matter but have low contamination by other gamma-ray sources. Finally we can get observations of dark matter dense regions is to observe regions around intermediate-mass black holes with masses in the range $10^2 \leq M/M_\odot \leq 10^6$, since there are enhancements (mini-spikes) of the dark matter densities around these black holes [33]. In the sections below we will discuss specific gamma-ray telescopes and their efforts in dark matter research.

2.3.1 Fermi-LAT

Most of our knowledge of gamma-ray emission from dark matter annihilation comes from the Fermi-LAT telescope. The non-detection⁴ of gamma-rays from dark matter annihilation has allowed us to put strong bounds on the dark matter parameters. The LAT, which stands for Large Area Telescope, is the primary instrument on the Fermi Gamma-ray Space Telescope mission. It has a wide field-of-view for high-energy gamma-rays and it covers the range from below 20 MeV to more than 300 GeV [34]. The Fermi-LAT telescope is able to directly detect the gamma-ray emission from dark matter annihilation. Observations of the Milky Way halo with Fermi-LAT provided some of the strongest constraints on the mass and cross section of the dark matter particles [35].

Nowadays the best results come from the observation of dwarf spheroidal satellite galaxies (dSphs) of the Milky Way, which are some of the most dark matter dominated objects known. Also dSphs are quite dim sources, which means that a detection of a gamma-ray excess could with great certainty be ascribed to dark matter annihilation. The lack of detection of gamma-rays gives us an upper limit to the dark matter cross section. Section 2.1 explains how the flux is related to the cross section. The newest Fermi-LAT data provide some of the most robust constraints on the dark matter mass.

For the $b\bar{b}$ annihilation channel the Fermi-LAT constraint is given by $m_{DM} \gtrsim 1$ TeV and the dark matter cross section $\langle\sigma v\rangle \lesssim 1 \cdot 10^{-26} \text{cm}^3 \text{s}^{-1}$, for the $\tau\tau$ channel they find $m_{DM} \gtrsim 70$ GeV and the dark matter cross section $\langle\sigma v\rangle \lesssim 4 \cdot 10^{-26} \text{cm}^3 \text{s}^{-1}$ [36]. The results are summarized in figure 7, where the confidence intervals in the mass - cross section plane are shown for the two annihilation channels ($b\bar{b}$ on the left and $\tau^+\tau^-$ on the right). The solid black line shows the observed limit from the combined analysis of 15 dSphs from [37]. The dashed gray curve in this figure corresponds to the thermal relic cross section from [38], which is expected from a dark matter freeze-out in the early Universe. The data points and circles in these plots represents claims of gamma-ray excesses from articles mentioned in the legend. These claims of dark matter mass and cross section can be excluded with this new data with 1σ confidence. The Fermi-LAT telescope will be able to further constrain the mass and cross section by observing the dSphs in longer observation runs and the discovery of new dSphs.

2.3.2 H.E.S.S.

Another important gamma-ray telescope is the H.E.S.S., which is an acronym for the High Energy Stereoscopic system. As opposed to the Fermi-LAT this is a ground based Imaging Atmospheric Cherenkov Telescope, which allows for much larger telescopes but also causes interference of the atmosphere with the gamma-ray detections. The H.E.S.S. collaboration shows a great evolution for constraints on the dark matter parameters over time. One of the first papers from 2006 concluded that there was no significant gamma-ray excess in the galactic center of the Milky Way [39]. In a 2011 publication they exclude cross sections larger than $\langle\sigma v\rangle = 3 \cdot 10^{-25} \text{cm}^3 \text{s}^{-1}$ for a dark matter mass of $m_{DM} \sim 1$ TeV [40]. The latest H.E.S.S. publication gives the strongest constraint on the dark matter cross section in for a $m_{DM} \sim 1$ TeV so far. The upper limit is given to be $\langle\sigma v\rangle = 4 \cdot 10^{-28} \text{cm}^3 \text{s}^{-1}$ [41].

⁴Claims of gamma-ray excess have been made in the past, see for example [1] and [2]. These claims of gamma-ray excesses have successfully been ascribed to other astrophysical sources.

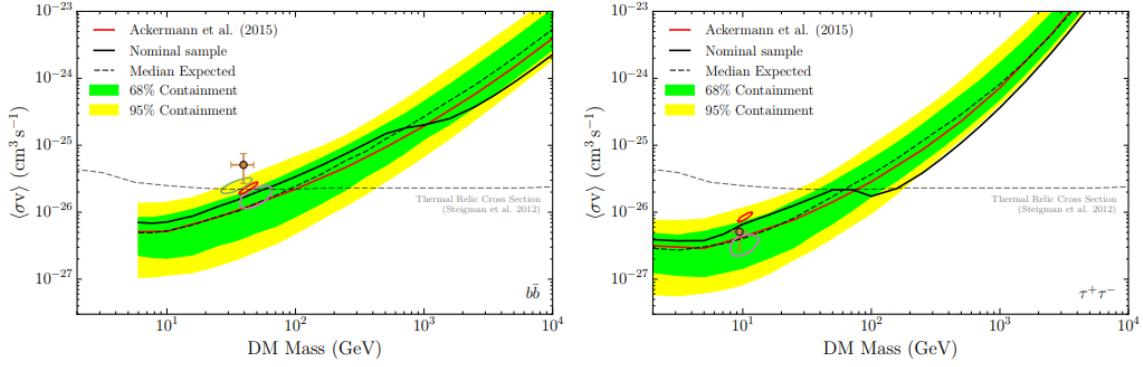


Figure 7: Figure from [36]: Constraints on the dark matter annihilation cross section at 95% CL for the $\chi\chi \rightarrow b\bar{b}$ (left) and $\chi\chi \rightarrow \tau^+\tau^-$ (right) channels derived from a combined analysis of 15 dSphs. Bands for the expected sensitivity are calculated by repeating the same analysis on 300 randomly selected sets of high-Galactic-latitude blank fields in the LAT data. The dashed line shows the median expected sensitivity while the bands represent the 68% and 95% quantiles. The solid black line shows the observed limit from the combined analysis of 15 dSphs from [37]. The dashed gray curve in this figure corresponds to the thermal relic cross section from [38].

2.3.3 VERITAS, MAGIC and HAWC

Other gamma-ray telescopes are also able to place constraints on the dark matter cross section, but these are usually less constrictive than the Fermi-LAT and the H.E.S.S. limits. VERITAS and MAGIC are both Imaging Atmospheric Cherenkov Telescope similar to H.E.S.S. but smaller in size. The HAWC is the High Altitude Water Cherenkov telescope, which uses water tanks to detect Cherenkov light from incoming gamma-rays as opposed to the atmosphere like H.E.S.S., VERITAS and MAGIC. The advantage of this technique is the ability to continuously run measurements at a wider field of view, instead of only at night (darkness is needed of atmospheric Cherenkov imaging). The latest VERITAS papers constrain the cross section for the bottom quark channel to $\langle\sigma v\rangle = 1.35 \cdot 10^{-23} \text{cm}^3 \text{s}^{-1}$ and for the tau lepton channel to $\langle\sigma v\rangle = 1.32 \cdot 10^{-25} \text{cm}^3 \text{s}^{-1}$ at $m_{DM} \sim 1 \text{ TeV}$ [42]. As said before the recent constraints from the H.E.S.S. collaboration are about 10^3 times more rigid. The MAGIC collaboration finds a strongest constraint in the tau lepton annihilation channel as well: $\langle\sigma v\rangle = 3.8 \cdot 10^{-24} \text{cm}^3 \text{s}^{-1}$ at $m_{DM} \sim 0.5 \text{ TeV}$ [43]. Finally there is HAWC which only started observing recently and therefore has not produced constraints nearly as strong as other telescopes yet [44].

2.3.4 Future telescopes

In the near future the Cherenkov Telescope Array (CTA) hopes to improve the current limits set by H.E.S.S. [45]. The CTA experiment will be the largest Imaging Atmospheric Cherenkov Telescope, taking into account telescope arrays in the northern and southern hemisphere. Since these telescopes vary in size, the CTA will improve sensitivity over a large energy range. They will be able to constrain the dark matter cross sections for dark matter masses ranging from 100 GeV to tens of TeV, with a sensitivity improved by a factor of 5-10 [45]. Fig. 8 shows how the CTA will hope to improve the dark matter cross section over a wide energy range. The sensitivity is shown in comparison with the strongest Fermi-LAT and H.E.S.S. constraints. It is important to note that these predictions are made by the CTA consortium itself. Critics of these optimistic constraints say that the actual CTA cross section constraints will be an order of magnitude weaker than estimated by the CTA consortium [46]. Here the galactic diffuse gamma-ray emission and systematic errors that will decrease the CTA sensitivity are properly taken into account.

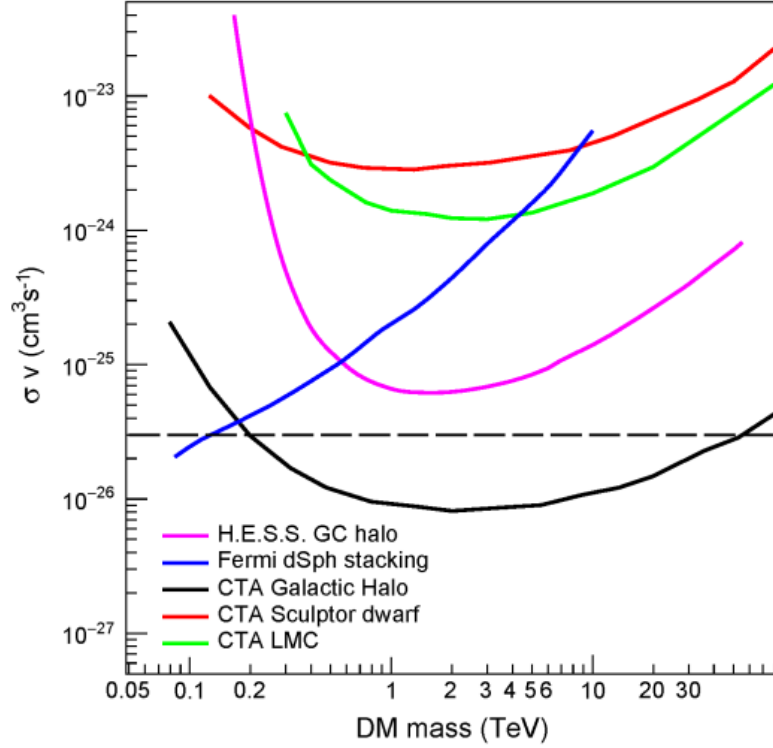


Figure 8: Figure from [47]: comparison of predicted sensitivities in for the targets of: the Milky Way Galactic halo: the Large Magellanic Cloud (LMC) and the dwarf galaxy Sculptor. The CTA sensitivity curves use the same method and W^+W^- annihilation modes for each target and the Einasto dark matter profile. The sensitivities for the three targets are all for 500 hours taking into account the statistical errors only.

Other planned gamma-ray telescopes include the CALET, GAMMA-400 and HERD. The first two telescopes have been launched recently and will improve the current resolution in small energy ranges [48, 49]. They will however not be able to improve the limits on the continuous spectrum, as set by Fermi-LAT. The HERD telescope is set to launch in 2020, and will be the most sensitive gamma-ray telescope in the 10 GeV to 1 TeV range [50]. At higher energies the Cherenkov telescopes will do better, since they have a larger effective area.

2.3.5 Comparison of gamma-ray telescopes

Table 1 shows a comparison of the discussed current (top) and future (bottom) gamma-ray telescopes in energy range, field of view, constraints on dark matter masses and cross sections.

Table 1: Comparison of different current (top) and future (bottom) gamma-ray telescopes in energy range, field of view (f.o.v.), constraints on dark matter masses and cross sections. The right column shows the references for these parameters. *: $\frac{2}{3}$ of the sky. **: these are the optimistic constraints as set by the CTA consortium. Critics thinks that the actual cross section constraints will be up to an order of magnitude higher [46]. ***:geometric factor $> 3m^2$ sr.

Name	Energy range	F.o.v (°)	m_{DM}	σv (cm^3/s)	Ref
Fermi-LAT	20 MeV - 300 GeV	4.2	~ 10 GeV	$\sim 4 \cdot 10^{-26}$	[34], [36]
H.E.S.S	300 GeV - 70 TeV	3.5	~ 1 TeV	$4 \cdot 10^{-28}$	[41]
Veritas	85 GeV - 30 TeV	3.5	~ 1 TeV	$2.85 \cdot 10^{-24}$	[42]
Magic	100 GeV - 100 TeV	3.5	~ 0.5 TeV	$3.8 \cdot 10^{-24}$	[43]
HAWC	500 GeV - 100 TeV	*	~ 1 TeV	$\sim 10^{-24}$	[44]
CTA	100 GeV - 10 TeV	4-5	~ 1 TeV	$5 \cdot 10^{-27} - 3 \cdot 10^{-26}$ **	[47], [45]
CALET	100 GeV - 1 TeV	45-58	—	—	[48]
GAMMA400	20 MeV - 1 TeV	60	—	—	[49]
HERD	10 GeV - 1 TeV	***	10 GeV 1 TeV	$6 \cdot 10^{-30} - 5 \cdot 10^{-29}$ $4 \cdot 10^{-27} - 9 \cdot 10^{-27}$	[50]

2.4 Smoking gun for the detection of dark matter annihilation - (Iris)

All gamma-ray measurements so-far have not detected any anomalies with respect to the astrophysical background. Therefore we have only been able to put constraints on the dark matter cross section and mass. If in the future technology allows us to reach sensitivities where we could actually probe the gamma-ray signal from dark matter annihilation, we could predict what this signal would look like. A smoking gun for a dark matter detection would be a spiked flux around a typical energy in a number of sources (for example multiple dwarf galaxies). This dark matter annihilation must be done via a leptonic channel, because otherwise the hadronization of the annihilation products allows for a variety of possible energy outcomes. Such a peaked flux usually lies at twice the annihilating particle's mass. So if a flux peak would be observed in multiple sources at an energy that is not compatible with any other standard model particle, we would have build have very strong case for a dark matter detection.

3 CMB constraints on dark matter

Another way to possibly detect dark matter is via its imprint on the Cosmic Microwave Background (CMB). Around the time of recombination ($z \sim 1000$) the secondary particles of dark matter annihilation would have affected other processes and therefore would have left an imprint on the CMB [51]. One of the biggest achievements of modern cosmology is the remarkable agreement between the theoretical description of recombination and the observations of the CMB. Our standard model of recombination is severely constrained by the CMB data, ie. changing the recombination model while staying in agreement with the CMB data has proven difficult [52]. Examples of refinements to the current recombination model are delayed recombination [53] and accelerated recombination [54], both of which turned out to correspond badly with the available CMB data. Measurements of the CMB by WMAP and more recently by Planck are able to put constraints on dark matter models.

3.1 Cosmological history with the CMB power spectrum - (Iris)

Figure 9 shows the theoretical CMB power spectrum, compared to the most recent Planck data [55]. As said before, one of the greatest achievements of modern cosmology is the remarkable agreement between our current Λ CDM model (red) and data (blue). We can even use this agreement to constrain the dark matter cross section. To do so it is important to fully understand the (bumps in the) CMB power spectrum and how they are affected by altering the theoretical input.

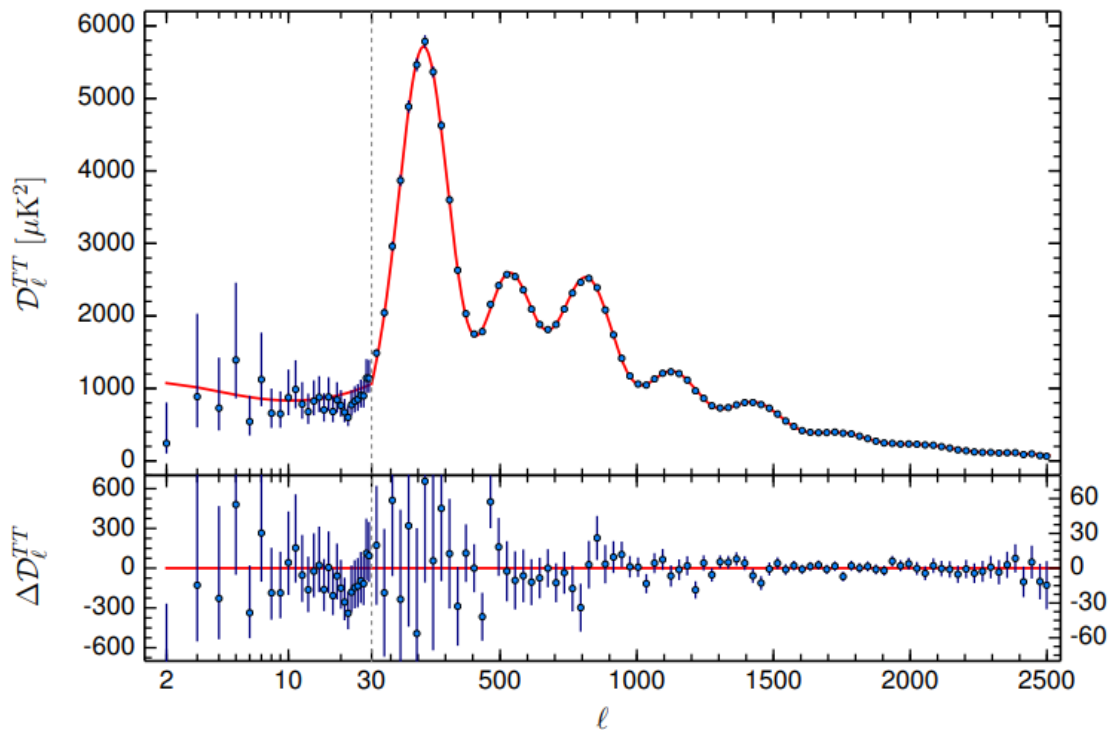


Figure 9: Planck 2015 CMB spectra, compared with the base Λ CDM fit to Planck data (red line). The upper panel show the spectra and the lower panel shows the residual. The horizontal scale changes from logarithmic to linear at the “hybridization” scale, $\ell = 29$. We show $D_\ell = \ell(\ell + 1)C_\ell/(2\pi)$ as a function of the angular scale ℓ . [55]

The Cosmic Microwave Background is a faint glow of the era of decoupling of the early Universe (380000 years after the Big Bang). At this point in time the temperature of the Universe had dropped enough for electrons and protons to form hydrogen and the Universe became opaque to photons. This afterglow of recombination nowadays has an average temperature of 2.725 K, but small fluctuations are present. Figure 9 shows the angular power spectrum of these temperature fluctuations. It shows that the angular fluctuations with the largest amplitude lie around $\ell = 200$. At higher ℓ the amplitude peaks again at around $\ell = 700$ and $\ell = 850$, which implies that temperature fluctuation at this angular scale are louder than other angular scales. These peaks in the power spectrum give valuable information about the physics in the early Universe.

The first peak shows the imprint and oscillation pattern of sound waves in the baryon fluid in the early Universe. This fluid was affected by gravity and radiation pressure, which respectively pulled the fluid together and pushed it away. The pushing and pulling of radiation and gravity causes a profound oscillation pattern. The way this oscillation pattern is found in the CMB is affected by the curvature of the Universe. In a closed Universe the light from hot spots (large amounts of matter at the time of decoupling) will bend in such a way that they appear larger in the CMB, and vice versa. Comparing our expectations of the oscillation pattern at this scale and observations of the CMB we find that our Universe is flat [55].

The second and third peak contain information about the amount of regular and dark matter in the Universe. At these scales the oscillating pattern is being damped. This damping is due to diffusion of photons at the time of decoupling from matter. This decoupling process was not instantaneous but took a few tens of thousands of years. During this period, photons and other particles were still interacting, though not as frequently as before decoupling. This small interaction rate scattered the photons and therefore damped the imprint of the oscillation pattern at small scales. The amount of damping of the second and third peak compared to the first, gives insight in the amount of baryonic and dark matter in the Universe.

After decoupling of photons from matter, the Universe began its so-called Dark Age. This epoch is called Dark since there were only two radiation sources. One was the slowly redshifting CMB, the other were photons occasionally released by neutral hydrogen atoms. The latter mechanism is known as the 21 cm line of hydrogen. During the Dark Ages gravity was acting on matter to clump it in high density regions, that were able to form stars and galaxies. The Dark Ages slowly evolved into the next epoch, where actual stars and galaxies gradually formed. This led to the event over reionization: the radiation of the first stars reionized the surrounding Universe. Neutral hydrogen atoms were split into a plasma of electrons and protons again. During this reionization the Universe remained largely transparent, and this epoch ended slowly due to the expansion of the Universe.

3.2 Dark matter annihilation at recombination - (Iris)

The structure and equations of this section are based on [51] and [56]. The annihilation of dark matter particles affects the ionization history of the Universe in three different ways. The interaction of the decay shower from the annihilation products with the thermal gas can either ionize the gas, induce a Ly- α excitation of hydrogen or simply heat the plasma. Figure 10 schematically shows the possible outcomes of dark matter annihilation. In this discussion we neglect the neutrino contribution, since they do not interact with the inter galactic medium (IGM). Ionization and Ly- α excitation influence the evolution of the free electron fraction x_e , while the heating of the plasma only affects the baryon temperature. Adjusting the expression for the evolution of the ionization fraction x_e for annihilation particles we find:

$$\frac{dx_e}{dz} = \frac{1}{(1+z)H(z)} [R_s(z) - I_s(z) - I_\chi(z)] \quad (12)$$

where R_s is the standard recombination rate, I_s the ionization rate by standard sources, and I_χ is the new term that accounts for the ionization rate due to particle annihilation. The first two terms are standard expressions, available in most CMB codes. See for example [57] and [58] which are based on [59].

The interesting addition to this equation is the ionization rate due to in this case the annihilation of dark matter particles. This ionization rate happens both by direct ionization from the ground state ($I_{\chi_i}(z)$) and by adding additional Ly- α photons to the plasma ($I_{\chi_\alpha}(z)$). These photons will increase the rate of photo-ionization by the CMB from the excited states. Therefore I_χ can be split up into two parts $I_\chi(z) = I_{\chi_i}(z) + I_{\chi_\alpha}(z)$.

The power output per unit volume by a self-annihilation dark matter particle is given by

$$\frac{dE(z)}{dVdt} = \rho_c^2 c^2 \Omega_{DM}^2 (1+z)^6 f \frac{\langle \sigma v \rangle}{m_\chi} \quad (13)$$

As before $\langle \sigma v \rangle$ is the effective velocity averaged cross section of the dark matter particle with mass m_χ . Ω_{DM} is the dark matter density parameter, ρ_c is the critical density of Universe today and the f parameter indicates the energy fraction that is absorbed overall by the gas. From here it is possible to relate $I_{\chi_i}(z)$ and $I_{\chi_\alpha}(z)$ to the power output:

$$\begin{aligned} I_{\chi_i} &= C \chi_i \frac{[dE/dt]}{n_H(z) E_i} \\ I_{\chi_\alpha} &= (1 - C) \chi_\alpha \frac{[dE/dt]}{n_H(z) E_\alpha} \end{aligned} \quad (14)$$

Here $\chi_i = \chi_\alpha = (1 - x_e)/3$ are the fractions of energy going to ionizations and Ly- α photons respectively, $n_H(z)$ is the number density of hydrogen nuclei, E_i is the average ionization energy per baryon and E_α is the difference in binding energy between the 1s and 2p energy levels of a hydrogen atom. Incorporating formula 13 and 14 in formula 12 yields a simple extension with the dark matter ionization rate to the standard evolution of the ionization fraction.

This extension of the ionization fraction is useful since we can compare it to current models and data and find how big certain dark matter parameters (such as $\langle \sigma v \rangle$ and m_χ) can be before we find significant deviations from the CMB angular power spectrum. Therefore we can place upper limits on these parameters.

3.3 Sommerfeld enhancement - (Iris)

An example of the contribution of CMB analysis to our understanding of dark matter is the exclusion of Sommerfeld enhancement. In 2008 a positron excess was observed by the PAMELA satellite [61]. This excess was attributed to the signature of dark matter annihilation, where the dark matter cross section had to be enlarged via the Sommerfeld enhancement [62, 63]. In more recent work by [64] it is shown that dark matter annihilation can not be the cause of the positron excess. They conclude this based on the limits from the μ -type distortion of the CMB energy as observed by the FIRAS (Far Infrared Absolute Spectrophotometer) instrument on the COBE (Cosmic Background Explorer) satellite.

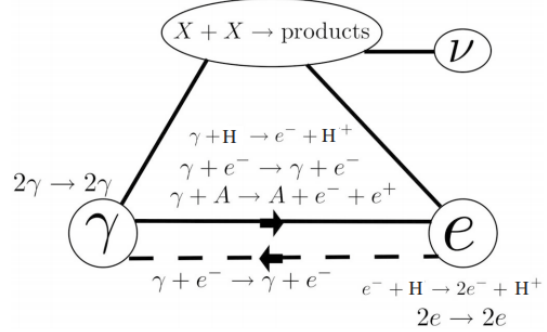


Figure 10: Figure from [60]: The injection of energy from dark matter annihilation into the IGM, via the creation of electromagnetic cascades. Energy transfer to the IGM takes place principally through the ionization and collisional processes.

3.4 Cosmological signatures of dark matter self-annihilation - (Bouke)

Having discussed the theoretical link between dark matter annihilation and the thermal history of the Universe, we have all the tools we need to investigate potential footprints of the involved dark matter processes within acquired observational data. Of particular interest are the observations procured by the Planck satellite between 2009 and 2013. Having provided the highest sensitivity mappings of CMB anisotropies to date, this satellite has enabled researchers to put stringent upper limits on dark matter effective self-annihilation rates. Not surprisingly, in recent years we have seen the publication of several papers dedicated towards constraining dark matter annihilation parameters via Planck satellite data [65, 66]. This subsection is dedicated towards summarizing some of the most important findings.

3.4.1 Methodology

Before diving into the various results on dark matter self-annihilation derived from cosmic microwave background data over the last years, let us first recapitulate on the methodology often applied in CMB indirect DM searches. In section 3.2 we saw that dark matter annihilation holds considerable sway over the course of cosmological history in the sense that the process may have injected vast amounts of energy into the intergalactic medium (IGM) at certain redshifts. From an observational point of view, this is important, since it might have lead to detectable defects in a diverse range of cosmological measurements, such as the baryonic matter and dark matter densities, the CMB angular power spectrum, the temperature of the intergalactic medium, as well as the optical depth towards the epoch of reionization. Of particular relevance to induced changes in all of these parameters, is the quantity:

$$p_{ann} \equiv f \frac{\langle \sigma v \rangle}{m_\chi} \quad (15)$$

which was already encountered in equation 13. Since p_{ann} is directly coupled to the dark matter annihilation ionization rates by virtue of equation 12, the parameter will cause different evolution schemes of the free electron fraction x_e for different values. In the literature this is often modeled using the recombination coding routine *RECFAST* [67].

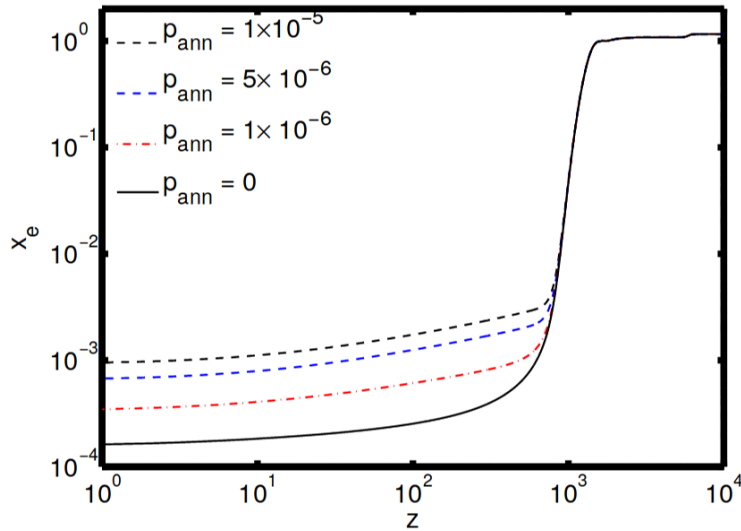


Figure 11: The evolution of the free electron fraction as a function of redshift for different values of p_{ann} , as presented in Galli et al. (2009) [51].

Figure 11 displays the evolution of x_e for different values of p_{ann} . Evidently, values as small as $p_{ann} = 1 \times 10^{-5}$ can introduce up to an order of magnitude difference in the ionization fraction at redshifts $z < 10^3$ (before the epoch of recombination). This goes to show the impact that dark matter annihilation can have on cosmological history.

In close correspondence with the free electron fraction, the CMB angular power spectrum will also vary between different values of p_{ann} . This is perhaps best understood by looking at optical depth. If the number density of free electrons is indeed enhanced by dark matter self-annihilation, the optical depth towards the last scattering surface of the CMB photons will naturally increase. As a consequence we will have to deal with a larger opacity when measuring the CMB, causing the amplitude in the angular power spectrum to decrease.

Figure 12 displays how the temperature (TT) and E-mode polarization (EE) CMB angular power spectra as well as the temperature and E-mode polarization cross spectrum (TE) vary for different dark matter annihilation schemes. As we predicted earlier, the acoustic oscillations within the angular power spectra become damped whenever there is a non-trivial dark matter annihilation rate. More interesting to note is the fact that there exists little difference between the curves with equivalent values of $\langle \sigma v \rangle / m_\chi$. This has to do with the fact that the f-parameter in equation 15 varies very little over the redshift range where scattering of CMB-photons is most likely (i.e. between around $z \sim 800$ and $z \sim 1200^5$). As a consequence, the acoustic oscillations of the power spectra are only truly affected by the average value of f around $z \sim 1100$, which happens to be nearly equal for all dark matter WIMP candidates with equal annihilation-rate-to-mass ratio $\langle \sigma v \rangle / m_\chi$.

In order to formulate a definitive answer to the question which model for dark matter annihilation holds the most merit (i.e. which value of p_{ann} yields the most sensible numbers for CMB observables), one has to confer with observational data in some way or another. Usually this is accomplished via a series of maximum likelihood fits to the parameters:

$$\{\Omega_{b,0}h^2, \Omega_{DM,0}h^2, \Theta_s, z_{reio}, n_s, \ln[10^{10}A_s], \langle \sigma v \rangle, m_\chi\} \quad (16)$$

where $\omega_b \equiv \Omega_{b,0}h^2$ stands for the baryonic matter density, $\omega_{DM} \equiv \Omega_{DM,0}h^2$ denotes the dark matter density and Θ_s describes the ratio between the angular sound horizon and the angular diameter to decoupling⁶. Furthermore, z_{reio} stands for the redshift to the start of reionization, n_s indicates the scalar spectral index, $\ln[10^{10}A_s]$ indicates the logarithmic amplitude of the primordial power spectrum⁷, $\langle \sigma v \rangle$ denotes the thermally-averaged dark matter annihilation cross section and m_χ describes the dark matter mass. A Markov Chain Monte Carlo (MCMC) analyzation method allows one to sample values for each of the cosmological parameters ω_b , ω_{DM} , Θ_s , z_{reio} , n_s and A_s , such that WMAP and PLANCK CMB observational data are fitted best.

In figure 13 we see the constraints derived by Galli et al. for the baryonic and cold dark matter density as well as the scalar spectral index using the five-year WMAP satellite data in 2009. Although the cold dark matter density does not seem to be affected by the inclusion of dark matter annihilation, the baryonic matter density and the scalar spectral index are clearly subjected to a shift. For an upper limit $p_{ann} < 2.0 \times 10^{-6} \text{ m}^3/\text{s}/\text{kg}$ we see that the constraint on ω_b changes from $\omega_b = 0.0228 \pm 0.0006$ to $\omega_b = 0.0230 \pm 0.0006$, whilst the limits on n_s change from $n_s = 0.965 \pm 0.014$ to $n_s = 0.977 \pm 0.018$.

⁵This is explained in more detail Hütsi et al. (2011) [68]. In particular, see the sharp peak of the visibility function around $z \sim 1100$ in figure 2 of the same paper.

⁶With the *sound horizon* we refer to the characteristic length scale of the CMB accoustic oscillations, which are given by the comoving distance that a sound wave can travel between the Big Bang and recombination [70].

⁷The *scalar spectral index* n_s and the amplitude A_s usually come up when discussing primordial density fluctuations. In this context, the power in density fluctuations with wavenumber k is generally assumed to behave as $P(k) = A_s(k/k_*)^{n_s-1}$, where $k_* = 0.05 \text{ Mpc}^{-1}$ denotes a reference scale and where $n_s = 1$ corresponds to a situation of *scale-invariant* fluctuations.

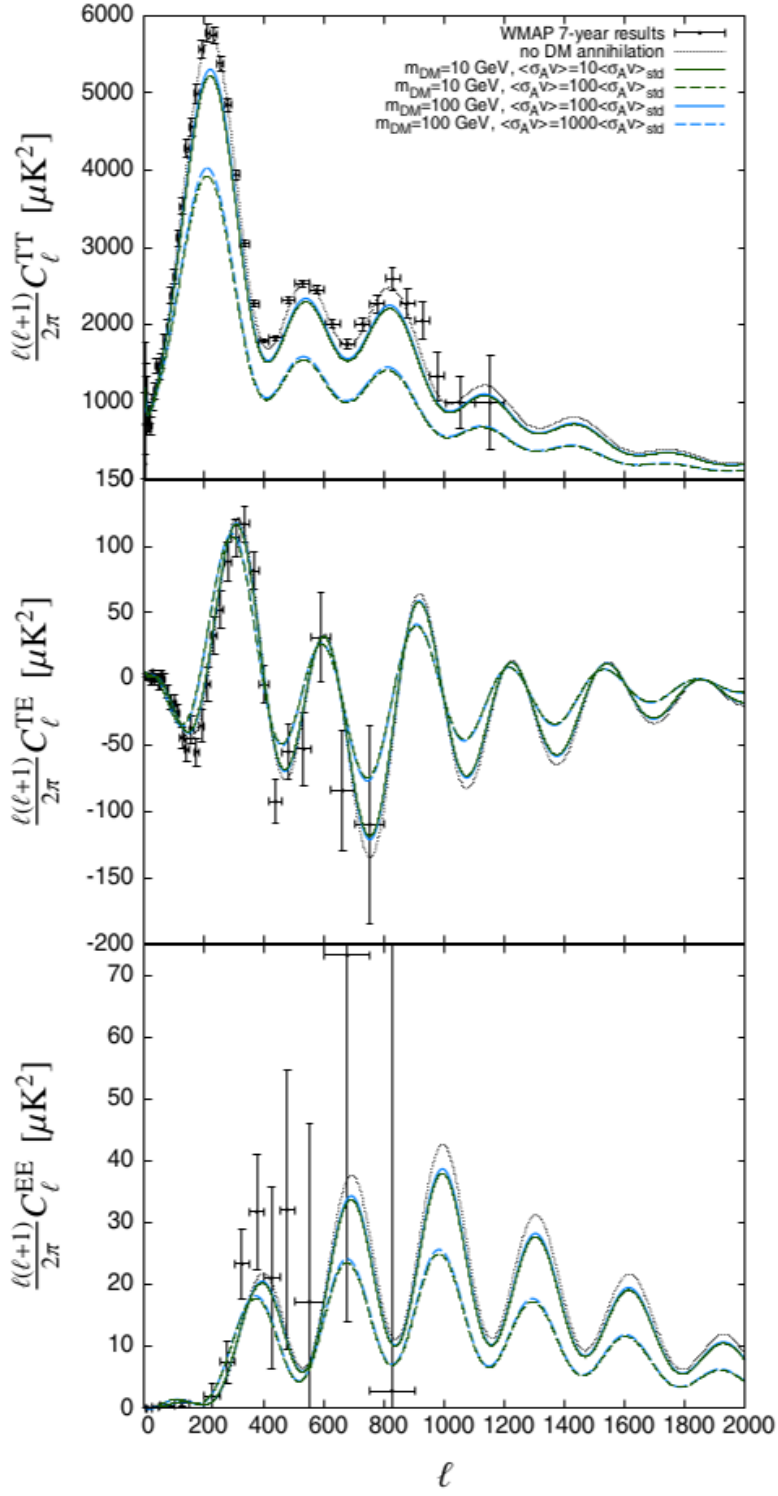


Figure 12: Angular power spectra of the CMB as presented in Hütsi et al. (2011) [68] for different dark matter masses and annihilation rates. From top to bottom we have (i) the angular power spectra derived for the CMB temperature anisotropies, (ii) the temperature and E-mode polarization cross-spectra and (iii) the E-mode polarization spectra. Dotted lines show theoretical predictions for the Λ CDM model [69], whilst the points with errorbars indicate 7-year measurements conducted by the WMAP space mission.

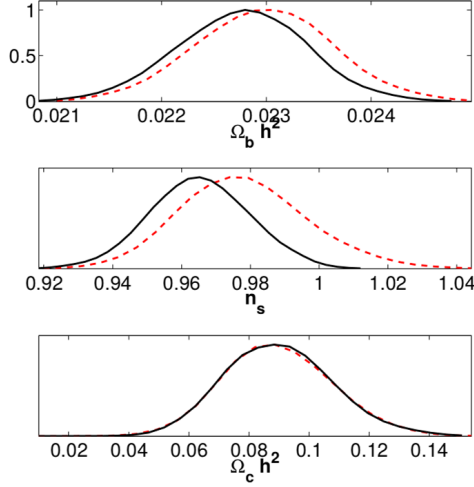


Figure 13: The 1-D likelihood distributions of the baryonic matter density, the scalar spectral index and the cold dark matter density as derived in Galli et al. (2009) [51] using the five-year WMAP dataset. Solid lines indicate results in the case of standard recombination, whilst dashed lines show constraints including dark matter annihilation.

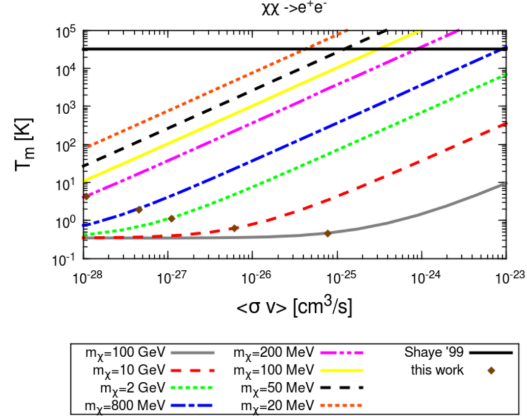


Figure 14: Dark matter annihilation constraints on the IGM temperature T_m as presented in Lopez-Honorez (2013) [71], assuming annihilation occurs into e^+e^- pairs solely and $z_{reio} = 10$. Brown diamond indicate upper limits obtained for $\langle \sigma v \rangle$ using WMAP9+SPT11+HST+BAO data, whilst a black solid line shows the $T_m = 32000$ K upper limit derived from Ly- α observations at $2 < z < 4.5$.

Some more recent papers, incorporating the latest data by WMAP and PLANCK give constraints on $\ln [10^{10} A_s]$ and the IGM temperature T_m , similar to the ones discussed above for n_s , ω_b and ω_c . Of particular interest are figures 14 and 15, which can be found in Lopez-Honorez (2013) [71] and in Madhavacheril et al. (2014) [66] respectively. As can be seen, lower dark matter particle masses and higher annihilation rates lead to higher IGM temperatures. This makes sense, considering that greater values of p_{ann} lead to increased energy injection rates, as we saw previously in equation 13. Another interesting fact to note is that the dark matter annihilation rate decreases, whenever the dark matter particle mass goes down (see the brown datapoints in the plot). This is of course caused the decrease in energy phase space, which makes the annihilation process less efficient.

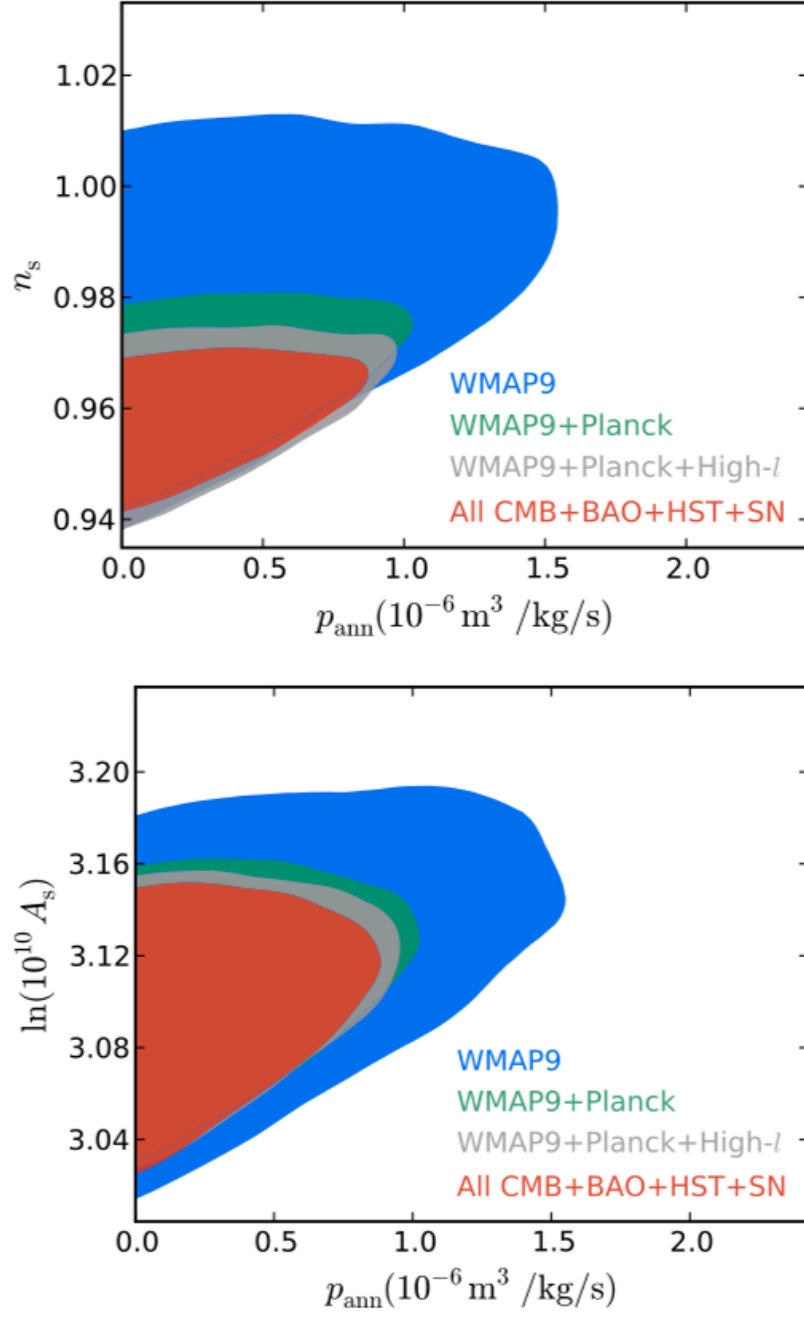


Figure 15: 95% confidence limit contours for n_s and $\ln [10^{10} A_s]$ as a function of p_{ann} as derived by Madhavacheril et al. in 2014 [66] for selected combinations of datasets.

3.5 Observational constraints of self-annihilation cross section from WMAP and PLANCK data - (Paul)

From the constraints on p_{ann} that come from maximum likelihood parameter fitting (see chapter 3.4.1) and using equation 15, we find the following velocity averaged annihilation cross section $\langle \sigma v \rangle_r$ at recombination as a function of dark matter mass m_χ , see figure 16. Note that f the coupling between the galactic gas with the dark matter annihilation product depends on multiple less understood factors; composition of the shower, its energy spectrum and most likely on the properties of the dark matter particles itself. In figure 16, the coupling factor is set to $f = 0.5$, which seems to be a good average approximation over different channels by [51]. It is clear that finding these constraints for different values of f should not be a problem, and is therefore less relevant.

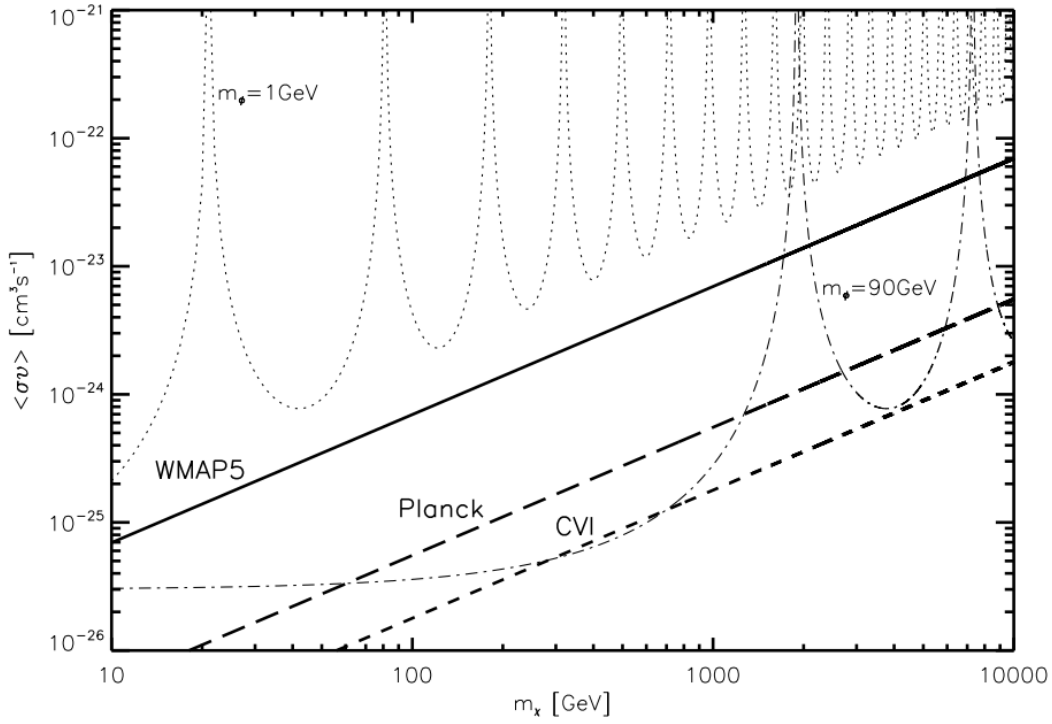


Figure 16: Figure from [51]. Velocity averaged annihilation cross section $\langle \sigma v \rangle_r$ at recombination as a function of dark matter mass m_χ , with the coupling parameter $f = 0.5$. Where the thin dashed lines are constraints from Sommerfeld enhanced cross sections (for two different boson masses $m_\phi = 1 \text{ GeV}$ and $m_\phi = 90 \text{ GeV}$) and the thick lines are constraints from WMAP and predicted Planck data and its Cosmic Variance Limited case.

The thin dashed lines correspond to the constraints by the Sommerfeld enhancement (SE), which enhances the self-annihilating dark matter cross section to explain the positron excess mentioned before (see chapter 3.3). This has been plotted for two different force carrier boson masses ($m_\phi = 1 \text{ GeV}$ and $m_\phi = 90 \text{ GeV}$). The resonating form of the constraints is due to the Sommerfeld enhancement solution being saturated at low velocity ($\beta \sim m_\phi/m_\chi$), see formula 17.

$$SE(\beta) = \frac{\alpha\pi}{\beta} \left(1 - e^{-\alpha\pi/\beta} \right) \quad (17)$$

The thick black line describes the constraints found from the WMAP5 data (2009) [72] and their maximum likelihood fits of the parameters found in 16. Comparing this to the thermal relic cross

section $\langle \sigma v \rangle = 3 \cdot 10^{-26} \text{cm}^3/\text{s}$, no dark matter mass is excluded since the probed region ($10 - 10000 \text{GeV}$) lies entirely above this values. It does exclude most of the Sommerfeld enhancements in the boson mass range of a few GeV. We can summarize the WMAP5 constraints by the following upper limit cross section:

$$\sigma v_{z_r}^{max} = 71.2 \cdot 10^{-26} \left(\frac{p_{ann}^{max}}{2.0 \cdot 10^{-6} \text{m}^3 \text{s}^{-1} \text{kg}^{-1}} \right) \left(\frac{m_\chi}{100 \text{GeV}} \right) \left(\frac{0.5}{f} \right) \quad (18)$$

Where $\sigma v_{z_r}^{max}$ is the upper limit on the velocity averaged self-annihilation cross section in terms of p_{ann} equation 15, m_χ the dark matter WIMP mass and f the coupling factor.

A prediction of the probe qualities of Planck (2015) is plotted as the thick long dashed line. Planck data is discussed more in-depth below. The Cosmic Variance Limited (CVL) case with comparable angular resolution as Planck, is also plotted and denoted as the thick short dashed line. In the CVL case, uncertainty due to only measuring one cosmic microwave background, are ignored which almost differ a order of magnitude with the real constraints. Figure 16 also shows that for increasing dark matter mass m_χ , the cross section also goes up as you would expect from equation 18. In the previous method of detecting dark matter (see chapter 2) we saw that probing higher masses is difficult due to a low gamma-ray flux.

3.5.1 WMAP

The Wilkinson Microwave Anisotropy Probe (WMAP) launched on a spacecraft in 2001 by NASA into a lunar assisted trajectory (see Appendix 6.1) and was the successor of COBE. It was planned to observe the CMB fluctuations for 24 months, which was subsequently extended to almost 10 years. The passively cooled microwave radiometers measure the temperature difference of the CMB between two different points in the sky and compares them directly. This method is more accurate than measuring absolute values and allows WMAP to probe up to 0.0002K differences over a frequency range of $23 - 94 \text{GHz}$ (see NASA website [73]). It's 5 year run data (WMAP5) provides stringent constraints on the parameters of the minimal ΛCDM model [72], which are shown in figure 17. The uncertainties on these parameters are partly due to instrumental effects but largely due gravitational lensing by inhomogeneous mass distributions in or along the line of sight.

Some of the parameters mentioned in 16 can be directly found in figure 17; Hubble constant H_0 and h , baryonic matter density Ω_b , dark matter density Ω_c , scalar spectral index n_s and the z value of reionization z_{reion} . Also found in [72] is the amplitude of the primordial power spectrum $A_{ps} = 0.0011 \pm 0.001 \mu \text{K}^2 \text{sr}$, they leave the parameters $\langle \sigma v \rangle_r$ and m_{DM} to others.

SUMMARY OF THE COSMOLOGICAL PARAMETERS OF Λ CDM MODEL AND THE CORRESPONDING 68% INTERVALS

Class	Parameter	WMAP 5-year ML ^a	WMAP+BAO+SN ML	WMAP 5-year Mean ^b	WMAP+BAO+SN Mean
Primary	$100\Omega_b h^2$	2.268	2.262	2.273 ± 0.062	$2.267^{+0.058}_{-0.059}$
	$\Omega_c h^2$	0.1081	0.1138	0.1099 ± 0.0062	0.1131 ± 0.0034
	Ω_Λ	0.751	0.723	0.742 ± 0.030	0.726 ± 0.015
	n_s	0.961	0.962	$0.963^{+0.014}_{-0.015}$	0.960 ± 0.013
	τ	0.089	0.088	0.087 ± 0.017	0.084 ± 0.016
	$\Delta^2_{\mathcal{R}}(k_0^e)$	2.41×10^{-9}	2.46×10^{-9}	$(2.41 \pm 0.11) \times 10^{-9}$	$(2.445 \pm 0.096) \times 10^{-9}$
Derived	σ_8	0.787	0.817	0.796 ± 0.036	0.812 ± 0.026
	H_0	72.4 km/s/Mpc	70.2 km/s/Mpc	$71.9^{+2.6}_{-2.7}$ km/s/Mpc	70.5 ± 1.3 km/s/Mpc
	Ω_b	0.0432	0.0459	0.0441 ± 0.0030	0.0456 ± 0.0015
	Ω_c	0.206	0.231	0.214 ± 0.027	0.228 ± 0.013
	$\Omega_m h^2$	0.1308	0.1364	0.1326 ± 0.0063	$0.1358^{+0.0037}_{-0.0036}$
	z_{reion}^f	11.2	11.3	11.0 ± 1.4	10.9 ± 1.4
	t_0^g	13.69 Gyr	13.72 Gyr	13.69 ± 0.13 Gyr	13.72 ± 0.12 Gyr

^aDunkley et al. (2008). “ML” refers to the Maximum Likelihood parameters^bDunkley et al. (2008). “Mean” refers to the mean of the posterior distribution of each parameter^cDunkley et al. (2008). “ML” refers to the Maximum Likelihood parameters^dDunkley et al. (2008). “Mean” refers to the mean of the posterior distribution of each parameter^e $k_0 = 0.002 \text{ Mpc}^{-1}$. $\Delta^2_{\mathcal{R}}(k) = k^3 P_{\mathcal{R}}(k)/(2\pi^2)$ (Eq. [15])^f“Redshift of reionization,” if the universe was reionized instantaneously from the neutral state to the fully ionized state at^g z_{reion} ^gThe present-day age of the universeFigure 17: Table from [72]. Maximum likelihood parameters of Λ CDM model by WMAP5, BAO and SN data set.

3.5.2 Planck

The successor of WMAP is named after the German Nobel prize winner; Max Planck. It is also the first probe send by the European Space Agency (ESA) which focuses on studying the CMB. Planck launched in 2009 and orbits the second liberation point (L2) just like WMAP did, see Appendix 6.1. Furthermore, Planck observers in a frequency range of $30 - 857 \text{ GHz}$ in nine frequency ranges instead of five for WMAP, which improve the astrophysical foreground models. Understanding the inhomogeneous mass distributions in and along the line of sight is quite important, since the measurement will be limited by how well the foreground can be subtracted. After a three year run, to following constraints on the Λ CDM model parameters were found [55]:

Parameter	PlanckTT+lowP 68% limits	PlanckTT, TE, EE+lowP 68% limits
$\Omega_b h^2$	0.02222 ± 0.00023	0.02225 ± 0.00016
$\Omega_c h^2$	0.1197 ± 0.0022	0.1198 ± 0.0015
$100\theta_{\text{MC}}$	1.04085 ± 0.00047	1.04077 ± 0.00032
τ	0.078 ± 0.019	0.079 ± 0.017
$\ln(10^{10} A_s)$	3.089 ± 0.036	3.094 ± 0.034
n_s	0.9655 ± 0.0062	0.9645 ± 0.0049
H_0	67.31 ± 0.96	67.27 ± 0.66
Ω_Λ	0.685 ± 0.013	0.6844 ± 0.0091
Ω_m	0.315 ± 0.013	0.3156 ± 0.0091

Figure 18: Table from [55]. Constraints on the cosmological Λ CDM model by Planck.

The results of WMAP and Planck agree with each other, but more impressive are the two to three order of magnitude improvements on the uncertainties of the parameters. Table 19 shows consistent output parameters under different maximal likelihood methods. These results also show a remarkable agreement considering different foreground approximations have been used [55].

Parameter	Plik	CamSpec	Hillipop	Mspec	Xfaster (SMICA)
$\Omega_b h^2$	0.02221 ± 0.00023	0.02224 ± 0.00023	0.02218 ± 0.00023	0.02218 ± 0.00024	0.02184 ± 0.00024
$\Omega_c h^2$	0.1203 ± 0.0023	0.1201 ± 0.0023	0.1201 ± 0.0022	0.1204 ± 0.0024	0.1202 ± 0.0023
$100\theta_{MC}$	1.0406 ± 0.00047	1.0407 ± 0.00048	1.0407 ± 0.00046	1.0409 ± 0.00050	1.041 ± 0.0005
τ	0.085 ± 0.018	0.087 ± 0.018	0.075 ± 0.019	0.075 ± 0.018	0.069 ± 0.019
$10^9 A_s e^{-2\tau}$	1.888 ± 0.014	1.877 ± 0.014	1.870 ± 0.011	1.878 ± 0.012	1.866 ± 0.015
n_s	0.962 ± 0.0063	0.965 ± 0.0066	0.961 ± 0.0072	0.959 ± 0.0072	0.960 ± 0.0071
Ω_m	0.3190 ± 0.014	0.3178 ± 0.014	0.3164 ± 0.014	0.3174 ± 0.015	0.3206 ± 0.015
H_0	67.0 ± 1.0	67.1 ± 1.0	67.1 ± 1.0	67.1 ± 1.1	66.8 ± 1.0

Notes. Each column gives the results for various high- ℓ TT likelihoods at $\ell > 50$ when combined with a prior of $\tau = 0.07 \pm 0.02$. The *SMICA* parameters were obtained for $\ell_{\max} = 2000$.

Figure 19: Table from [55]. Constraints on the cosmological Λ CDM model with Planck data, analyzed by different maximal likelihood methods.

To summarize their findings, figure 20 shows the velocity averaged annihilation cross section $\langle \sigma v \rangle_r$ times the coupling factor f at recombination as a function of dark matter mass m_χ . The blue area indicates the parameter space that is excluded by Planck data. Which exclude, when looking at the thermal relic cross section (red band), a dark matter mass $m_\chi < 44\text{GeV}$ for $f = 0.6$ and $m_\chi < 16\text{GeV}$ for $f = 0.12$ and $m_\chi < 11\text{GeV}$ for $f = 0.15$. Furthermore, the yellow lines denotes the constraints from the data by WMAP9 (where the 9 stands for nine year data taking run) and the dashed green lines denotes the CVL case for same angular resolution as Planck. The higher than thermal relic cross section induced by the Sommerfeld enhancement to explain the positron execs, are also excluded in dark grey. It is also notable that the predictions made by [51] are in agreement with the found constrains by Planck.

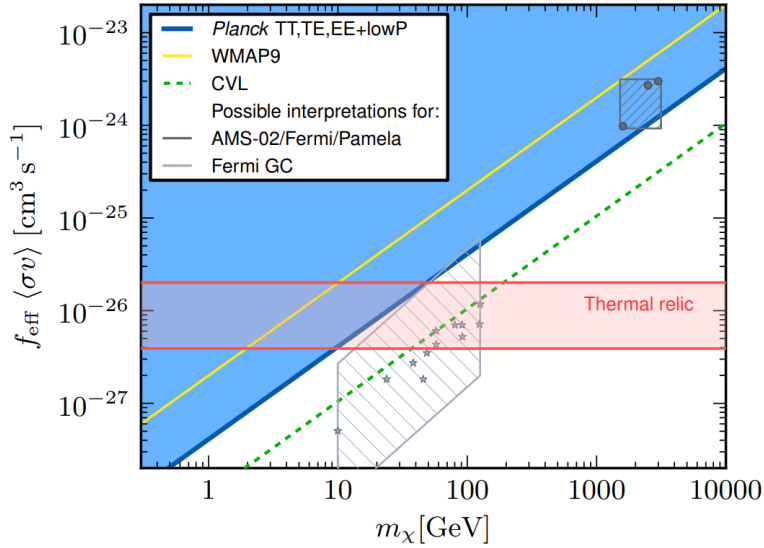


Figure 20: Figure from [74]. Velocity averaged annihilation cross section $\langle \sigma v \rangle_r$ times the coupling factor f at recombination as a function of dark matter mass m_χ by Planck. The blue area is the parameter space that is excluded by Planck, and the yellow denotes the same for WMAP9 data. The dashed green line corresponds to the CVL case, and the dark grey area shows the best-fit parameters to explain PAMELA/AMS-02/Fermi data. Lastly, the light gray area are the best fitted dark matter parameters for the Fermi Galactic data and the red band shows the thermal relic cross section times the coupling factor f .

4 Dark matter detection with anti-matter

In the previous sections of this review on indirect searches for dark matter, we focused our attention on signatures observable in the electromagnetic spectrum. So far we've looked at potential signals in the gamma-ray spectrum and in the CMB. However, with the construction of large new facilities for observing cosmic rays and neutrino's and with the recent confirmation of the existence of gravitational waves, it is important that we also look at non-EM observables. The following section will be dedicated to cosmic-ray dark matter signatures. In particular we'll explore how excess levels of positrons, antiprotons and anti-nuclei might be interpreted as secondary products of dark matter annihilation.

4.1 The Positron channel - (Bouke)

When the PAMELA collaboration published their results on the cosmic positron flux back in 2008, excitement was felt accross the entire astrophysical community: an excess signal above 7 GeV seemed to be compatible with expectations for dark matter annihilation, which would make PAMELA the first instrument to indirectly confirm the existence of dark matter WIMPS. How were scientists at the time so convinced of having found a dark matter signature? And why were the claims originally made, subsequently toned down? In the following section, an attempt is made to give an answer to both of these questions via analysis of recent literature. First, we'll discuss the general background of the problem, as well as the values one might expect to observe for the positron and electron+positron flux, both in case of the absence of dark matter and in its presence. Afterwards several different experimental results will be presented, which show how observations deviate from a pure background scenario. The final paragraphs will consist of an overview of several debates which ensued in the literature, contesting original the original claims made of dark matter indirect detection.

4.1.1 Expectations for the positron fraction and the electron + positron flux

The claim that there exists an 'excess' flux of positrons in observed cosmic ray spectra begs the question in which respect observed signals are in transgression. The answer is not immediately obvious and, consequentially, several authors have tried to explain the rising fraction of positrons as a spectral feature instead of a true anomaly [75]. To illustrate these different viewpoints, let us look at a more quantitative description of the problem. The positron fraction of cosmic rays can be modelled using the formula [76]:

$$f(E) \equiv \frac{1}{1 + (\Phi_{e-}/\Phi_{e+})} \approx \frac{1}{1 + \kappa E_{GeV}^\rho} \quad (19)$$

where the fluxes Φ_{e-} and Φ_{e+} for electrons and positrons signify values measured at the top of the atmosphere and where E_{GeV}^ρ denotes the fractional (power-law) energy spectrum of electrons versus positrons for spectral index ρ , with κ serving as the necessary constant of proportionality to fix dimensionality. Naively one would expect that all positrons are created as secondary cosmic-ray products from spallations and subsequent pion decays. As a consequence, the ratio between positrons and any cosmic-ray primary (either electrons or protons) should go down as energy increases. However, this does not correspond to what we observe.

Simple fits to PAMELA data (see the red points in figure 21) above 10 GeV⁸ yield $\rho = -0.38 \pm 0.06$ in case of the original analysis provided in 2009 [77], or $\rho = -0.23 \pm 0.04$ for the more recent analysis presented by the PAMELA collaboration in 2010 [78]. At the same time, fits to PAMELA electron data over the same energy interval show that $\Phi_{e-} \propto E^{-3.23 \pm 0.02}$, which would imply that $\Phi_{e+} \propto E^{-2.85 \pm 0.06}$ (or $\Phi_{e+} \propto E^{-3.00 \pm 0.04}$ in case of the 2010 analysis). However, if this is the case, the proton flux measured by PAMELA would be in disagreement. To understand this, it is important

⁸Incorporating data below this threshold would include charge-dependent solar modulation effects, which are detrimental to the accurate determination of the cosmic positron flux.

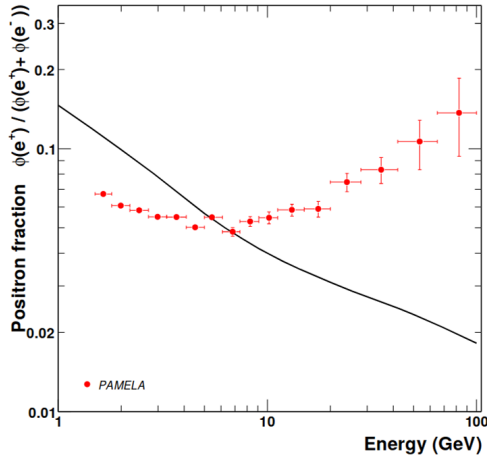


Figure 21: The PAMELA positron fraction as presented in the original 2008 PAMELA paper on the anomalous positron abundance [77]. A solid line indicates a theoretical prediction done by Moskalenko and Strong for pure secondary production of positrons during the propagation of cosmic rays through intergalactic space [82].

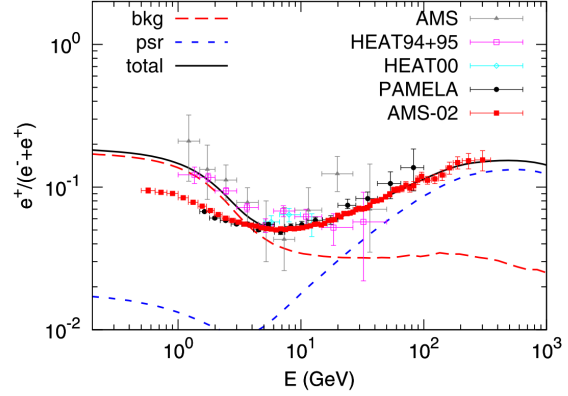


Figure 22: A more recent graph of the positron excess presented by Yuan and Bi in a 2013 paper [83], which incorporates the data acquired by the AMS-02 experiment. A model spectrum, composed of a pulsar-like element (blue dashed line) and expected background from standard cosmic-ray spallation (red dashed line) is indicated using a black solid.

to keep in mind that all ISM positrons trace their origins back to positrons. Hence, discrepancies between the spectral indices of these two particles suggest that there exists a population of primary positrons which do not derive from ordinary cosmic-ray spallation processes.

Recent PAMELA measurements of the positron flux indicate that the proton cosmic ray spectrum behaves as $\Phi_p \propto E^{-2.82}$. At first glance, this seems to be in reasonable agreement with the earlier stated spectral behaviour of Φ_{e^+} . However, propagation phenomena haven't been taken into account yet. These generally tend to cause spectral steepening and therefore cannot be kept out of the picture. Assuming, propagation happens via diffusive channels alone, one would expect to see the positron spectral index drop by about $\delta \approx 0.4$ [79]. In a recent numerical analysis conducted by J. Laval in 2011 [80] the positron cosmic ray flux is therefore situated at $\Phi_{e^+} \propto E^{-3.4}$ in the 10-100 GeV range, which clearly violates the spectral behaviour inferred from PAMELA observations. As a consequence, we often speak of an excess or 'anomaly' of positrons measured with respect to the expected positron fraction from numerical simulations. It is worthy to keep in mind, however, that the discrepancy between observational data and prospected values for Φ_{e^+} , may also be caused by some mistake in our current theoretical models for cosmic ray propagation. This would perhaps even offer for a breakthrough of greater extent than the addition of new primary cosmic ray sources. Nevertheless, despite several concerns raised with our current theoretical understanding of the problem [81], the notion of additional primary sources stands tall, since no propagation mechanisms are known which could steepen the positron spectrum between 10 GeV and 100 GeV by less than 0.2 with respect to its primary (i.e. proton) counterpart.

Assuming that the steepening of the positron spectrum above 10 GeV is not caused by any unknown propagation effects, the next question to tackle would of course be what phenomenon actually might be responsible for the measured excess. Over the years a variety of different explanations have come up. In 2009, Shaviv et al. proposed a model in which the surplus positron fraction may be attributed to a non-conventional shape of the electron flux, caused by e.g. the sum of a diffuse disk population and a local one [84]. However, even though it is likely that lepton propagation becomes

anisotropic at high energies (even below the TeV scale) this model is strongly disfavoured by present data (see for example the analysis given by J. Stockton in 2011 [85]). Hence, using Ockham's razor, the best (i.e. simplest and most conservative) explanation for the measured excess of positrons seems to be that there exists a population of primary positron accelerators.

Support for the primary positron accelerator scenario comes in the form of recent Fermi measurements. Besides detecting a positron spectrum harder than $E^{-3.0}$ in the range of interest [86], one component fits of Fermi data fail to reproduce both the total $e^+ + e^-$ flux and the e^+ flux. This suggests that proton contamination cannot be the main source of the observed anomaly. More importantly, however, it also provides support for the existence of an additional electron-positron production channel. In the following paragraphs we'll investigate the various astrophysical sources cited as potential sites for such production.

4.1.2 Dark Matter annihilation

The 2008 PAMELA collaboration release on the measured overabundance of positrons sparked a lot of interest in the particle physics community since 'excess' abundances of positrons are qualitatively expected in most dark matter annihilation models. As for the reason why the paper hasn't been unanimously brought forward as the first ever description of indirect dark matter detection, we can point at three observational caveats.

One of the main causes behind the ongoing debate surrounding the dark matter interpretation of the positron excess is given by the absence of a sharp spectral edge after the initial rise which is observed. In case the measured anomaly is indeed caused by dark matter annihilation, such an edge would be expected. However, it has not been observed as of present, neither in the e^+ fraction nor as a dip in the $e^+ + e^-$ data. A second cause for worry is provided by the surprisingly large normalization factor the dark matter contribution would be associated with, compared to predictions for typical S-wave annihilation thermal relics in agreement with observed dark matter abundances ($\langle\sigma v\rangle \gg \langle\sigma v\rangle_{th,S-wave} \approx 1$ pb). Thirdly, the large flux of electron-positron pairs observed by PAMELA implies the existence of similar excesses in the spectra of other high-energy particles, such as antiprotons, gamma-rays and possibly neutrinos, whilst no such anomalies have been yet revealed.

There are several ways to overcome the above difficulties, such that the dark matter annihilation picture can be maintained. The first is to increase the dark matter mass m_χ to values above the range accessible to PAMELA. Although this solves the first of the three mentioned problems, it may further complicate the second and third issues. After all, since the differential spectrum from dark matter annihilation scales as m_χ^{-2} (confer with equation 2.1 for a similar dependency in the case of the dark matter-induced gamma-ray flux), we would need an even higher annihilation rate $\langle\sigma v\rangle$ than before to achieve the same observational positron fluxes. Putting this aside for the moment, however, there are three ways in which the problem surrounding the exceptionally high annihilation rate may be remedied:

1. The first method is to attribute the high positron flux to a nearby clump of dark matter (as suggested in, for example, Hooper et al. (2009) [87]). In our current understanding of structure formation, however, this scenario seems very unlikely, especially given the constraints derived from gamma-ray fluxes in recent years.
2. The second option would be simply to accept that $\langle\sigma v\rangle \gg 1$ pb and try to explain the high value from an underlying physical process. One of the most popular methods cited in line with this approach, is the so-called Sommerfeld enhancement, which we also mentioned in the context of the previous chapter. Basically this enhancement constitutes an increase of the dark matter annihilation cross section as an effect of long-range (i.e. below TeV^{-1} scale) attractive forces, which are expected to operate within low-velocity (i.e. $v \approx 1 \times 10^{-3} c$ regimes). Several

alternatives to the Sommerfeld enhancement scheme include: a) non-thermal dark matter candidates, whose production is dictated by decays of other species and condensates rather than thermal freeze-out, b) a Breit-Wigner resonant enhancement [88] and c) a different theoretical framework for cosmological evolution of particle populations altogether. Take in mind that all of these options require some form of ad hoc parameter tuning,

3. The third solution is provided by positron production channels which originate from dark matter decay, instead of dark matter annihilation. Although this scenario may explain measured excesses quite neatly, it isn't favoured from an observational point of view, since the corresponding lifetime of $\approx 1 \times 10^{26}$ s required to fit the data cannot be predicted beforehand. Rather it has to be inferred a posteriori. Similar to the sec

Although a detailed analysis of the various considerations presented here, lies beyond the scope of this review, we should note that each model comes with a variety of different cavities of its own. The best way forward in pinning down the intricacies of dark matter annihilation seems to be to combine the different pictures and observational data that are currently available. Hence, good models for the positron excess should incorporate the stringent limits provided by the CMB, as well as current constraints derived from cosmic-ray fluxes.

4.1.3 Other potential sources: pulsars and pulsar wind nebulae

Although dark matter annihilation provides one of the most exciting explanations for the positron excesses measured by cosmic-ray observatories, it is possible to conceive of a variety of other phenomena resulting in the same behaviour. One of the most prominent alternative sources for positron cosmic-rays, often cited in the literature, are pulsars. Consisting of rapidly spinning, magnetized neutron stars with highly relativistic jets, these objects might constitute some of the primary loci of cosmic-ray leptons in the universe: since the objects have extremely high rotation rates, electrons are theorized to be kinematically stripped from the stellar surface under the influence of large induced tangential electric fields [89]. As a result, neutron stars are generally believed to be surrounded by spherical clouds of comoving plasma called "magnetospheres" up to typical distances known as the light radius $r_L = c/\Omega$. The electrons that end up within this sphere undergo radiative cooling (particularly via synchrotron radiation) and compton scattering, producing very high energy photons in the process. In turn, these ultra-high energy photons may contribute to pair-production, resulting in the formation of electron-positron pairs. The number of e^+e^- pairs is subsequently increased via a cascade of QED processes.

It is important to note that the e^+e^- pairs originally created as a consequence of photon annihilation and other QED processes, are not immediately the ones we observe with cosmic ray observatories on Earth. Although it's true that the pairs form an outwardly propagating wind together with the pulsar's poynting flux, the evolution scheme of the pulsar system is very involved and the amount of positrons actually escaping into the ISM is highly dependent on astrophysical considerations. For example, the pulsar system's geometry can be of great importance. Since pulsars are born out of core collapse supernovae, the magnetosphere lies within a capsule of particles ejected by the pulsar's predecessor which in turn exhibits a concentric, outwardly propagating blast wave. When the relativistic wind of particles emitted by the pulsar, comes into contact with this blast wave, two shock fronts are created, one of which propagates into the ISM, whilst the other reverses and travels backwards in the direction of the star. The latter of these two shock waves is called the *termination shock* and causes the pulsar wind to slow down, dissipating its bulk energy and turning it into a hot, relativistic fluid which is subsequently observed as a *pulsar wind nebula* (PWN).

The big question which we need to answer, of course, is to which extent a pulsar may be responsible for the positron excess. To do this, we need to quantify the positron energy spectrum a pulsar may generate. Our first observation, in this context, is going to be that, to a sufficient level of accuracy,

nearly all of the energy loss of a pulsar, can be attributed to rotational deceleration. Writing down the rotational frequency as Ω , this can be written as:

$$\dot{\Omega} = -\alpha\Omega^n \quad (20)$$

Using a spherical approximation, alongside the classical expression for rotational energy, we see that the spin-down luminosity is given by:

$$L = \left| \dot{E} \right| = I\Omega \left| \dot{\Omega} \right| = \alpha I\Omega^{n+1} \quad (21)$$

By solving equation 20 and substituting the result into equation 21, we get:

$$\Omega(t) = \frac{\Omega_0}{\left(1 + \frac{t}{\tau_0}\right)^{1/(n-1)}} \quad (22)$$

$$L(t) = \alpha I \frac{\Omega_0^{n+1}}{\left(1 + \frac{t}{\tau_0}\right)^{(n+1)/(n-1)}} \quad (23)$$

Here we introduced the characteristic timescale:

$$\tau_0 \equiv \frac{1}{\alpha(n-1)\Omega_0^{n-1}} \quad (24)$$

The above equations are still very general and are not pulsar-specific. To derive a formula which can easily be applied to a pulsar, we set $n = 3$ and $\alpha = 5B_s^2 R_s^4 / (8M_s c^3)$, which is the expression for a magnetic dipole of mass M_s . This yields:

$$E_{tot} = \frac{1}{2} I \Omega_0^2 \approx 2.2 \times 10^{46} \left(\frac{M_s}{1.4 M_\odot} \right) \left(\frac{R_s}{10 \text{ km}} \right)^2 \left(\frac{\Omega_0}{\text{Hz}} \right)^2 \text{ erg} \quad (25)$$

which typically gives a total energy $E_{tot} = 1 \times 10^{49}$ erg. Assuming a core-collapse supernova rate R_{CC} of about 2 per century in our Galaxy (see for example Diehl et al. (2006) [90]), this amounts to a maximum injected luminosity of:

$$L_{max} \approx 6.3 \times 10^{39} \text{ ergs}^{-1} \frac{R_{CC}}{2 \text{ century}^{-1}} \frac{E_{tot}}{10^{49} \text{ erg}} \quad (26)$$

Fits to observational data typically yield values which lie two orders of magnitude lower than the above upper limit [87, 91].

To derive the spectral behaviour of positron emission by pulsars, it is necessary to adopt models for the $e^+ - e^-$ acceleration as well as the escape probability. By integrating over a Monte Carlo sample of the pulsar parameters (i.e. magnetic field strength, rotational period, etc.) in a Galactic Pulsar population, the initially injected spectrum of positrons can be inferred. This typically leads to the numerically derived expression:

$$\frac{dN_e}{dE_e} \approx 8.6e38 \dot{N}_{100} (E_e/\text{GeV})^{-1.6} \exp(-E_e/80 \text{ GeV GeV}^{-1} \text{s}^{-1}) \quad (27)$$

where \dot{N}_{100} is the pulsar formation rate in units of pulsars per century (see Zhang et al. (2001) for the details [92]). Compared to the upper limit for the total luminosity which we derived earlier, this yields an average energy output of around 6×10^{46} erg per pulsar, i.e. about 1% of the total energy budget.

Of course the injected spectrum is not equal to the spectrum we observe on Earth. Propagation effects can be accounted for either by a leaky box model or, more scrupulously, by solving the transport equation for electrons with the inclusion of synchrotron and inverse Compton effects (see e.g. Hooper et al. (2009) [87]):

$$\frac{\partial}{\partial t} \frac{dn_e}{dE_e} = \vec{\nabla} \cdot \left[K(E_e) \vec{\nabla} \frac{dn_e}{dE_e} \right] + \frac{\partial}{\partial E_e} \left[B(E_e) \frac{dn_e}{dE_e} \right] + Q(E_e, \vec{x}) \quad (28)$$

where dn_e/dE_e denotes the number density of electrons with respect to positrons per unit energy, $K(E_e)$ stands for the diffusion coefficient, $B(E_e)$ is the rate of energy loss and where Q is given by the source term in equation 27.

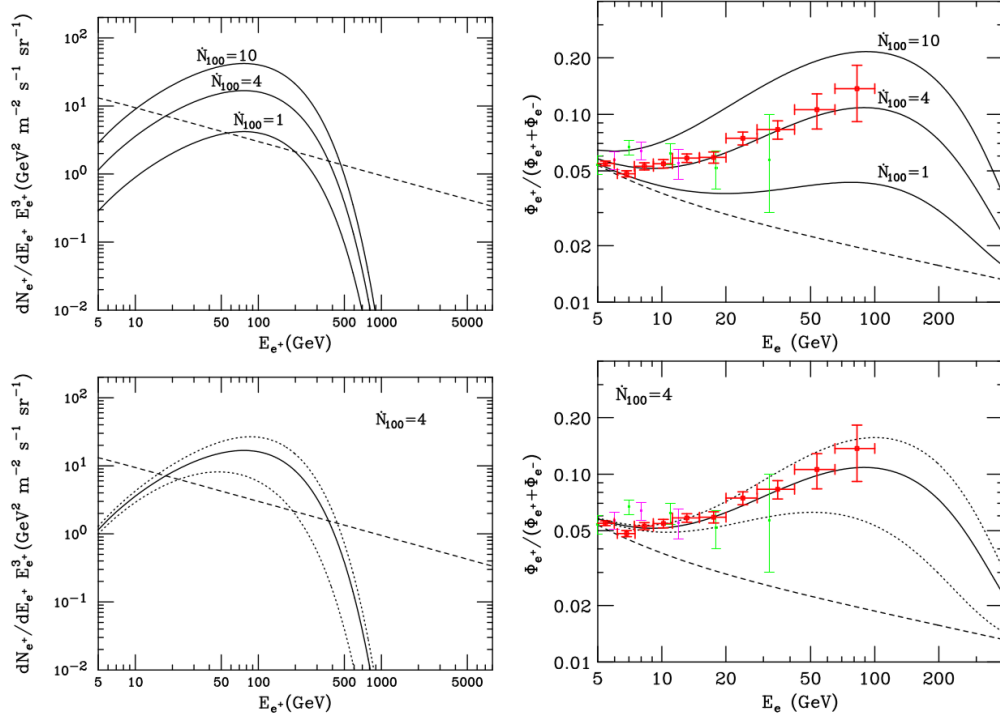


Figure 23: The spectrum of cosmic ray positrons (left) and the positron fraction (right) derived in Hooper et al. (2009) [87] using equation 28 for the sum of all pulsars throughout the Milky Way. In computing the spectrum, it was assumed that $K(E_e) \equiv K_0(1 + E_e/(3 \text{ GeV}))^\delta$ with $K_0 = 3.4 \times 10^{28} \text{ cm}^2 \text{ s}^{-1}$ and $\delta = 0.6$. Furthermore the diffusion coefficient was taken to be $B(E_e) = -bE_e^2$ with $b = 1 \times 10^{-16} \text{ GeV}^{-1} \text{ s}^{-1}$. A dashed line indicates the prediction for secondary positrons (primary and secondary electrons for the right panels) as derived by Moskalenko and Strong in 1998 [82]. Furthermore, the dotted lines in the lower frames indicate the case where the injection rate within 500 parsecs of the Solar System is doubled (upper dotted line) or neglected (lower dotted line). The right panels include the measurements of HEAT [93] and PAMELA [77].

Several spectra derived from equation 28 are shown in figure 23. Evidently, the measurements done by PAMELA and other cosmic ray observatories are well described by the pulsar origin model in case the pulsar formation rate is around 4 per century. This lies close to typical estimates for the galactic core collapse supernovae rate, from which pulsars originate (see e.g. Raffelt (2011) [94]). For this reason, among others, pulsars are often cited as likely alternative explanations for the positron excess. Note, however, that there are still many caveats involved with the pulsar model, which will have to be solved before the model can be completely accepted. For example, it is still quite unclear how the conversion from the initial pulsar Poynting flux-dominated outflow to the electron-positron wind

takes place. Furthermore, the hard low-energy part of the pulsar spectrum remains ill-understood with most theories assuming that the preponderance of non-thermal particles have low velocities.

On a final note, let us stress that dark matter annihilation and pulsar wind nebulae — although they constitute the currently most studied solutions — do not form the only potential explanations for the positron excess. Other models consider the production of positron-electron pairs in super nova remnants (SNRs) and e.g. accretion-powered X-ray binaries. We refer the interested reader to the review paper published by Serpico in 2012 [76], from which many of the above arguments were derived. If there is anything one should take home from the discussion we presented here, it's that the origin of the positron excess is still a highly debated problem to which no definite or unambiguous answer can be put forward as of yet. Potentially, energy-dependent positron anisotropy studies may exclude several of the proposed models. However, until our theoretical understanding of cosmic-ray escape from astrophysical objects improves, pinpointing specific sources for the positron excess will remain difficult.

4.2 Antiproton channel - (Iris)

Another way to search for dark matter annihilation is via the antiproton spectrum. Antiprotons can result either from the hadronization of primary quarks or gauge bosons or via electroweak radiation from leptonic channels. This idea is 30 years old already [95], but due to improvements in observations we are able to put stronger constraints on the dark matter parameters. In this section we will discuss the CR antiproton flux. The dark matter interpretations of the leptonic excesses (see section 4.1) are usually not favoured over explanations involving astrophysical sources [96]. In the interpretation of the CR antiproton flux, the secondary antiprotons have been shown to account for most of the measured flux [97]. This allows us to derive strong constraints on the dark matter contribution to the antiproton flux.

The Alpha Magnetic Spectrometer (AMS-02) onboard the ISS, is the most advanced detector of charged cosmic ray (CR) flux and therefore one of the best detectors in indirect dark matter experiments. Its most recent results provide the best measurements of the antiproton-to-proton flux ratio to date [98]. The new AMS-02 data furthermore improves the measurements of the proton spectrum and helium one. These measurements agree with previous publications by another CR flux detector, PAMELA [99], but are more precise and detailed. These two quantities are important ingredients in the computation of the secondary antiproton flux, which is the minimal astrophysical antiproton background in indirect dark matter research.

4.2.1 Astrophysical antiproton background

Secondary antiprotons are produced when CR high energy protons and helium nuclei collide with the interstellar medium. The interstellar medium consists mainly of hydrogen and helium, heavier nuclei corrections are only a few percent (see section 4.3). To compute the secondary astrophysical antiproton flux we require: i) the injection of proton and helium fluxes from Galactic sources ii) the collisional cross section and iii) the propagation details. For the proton and helium spectra the newest AMS-02 data are used. These measurements have some uncertainties that translate into the \bar{p}/p ratio, as shown in the blue uncertainty band of figure 24. The spectra are measured up to a rigidity ($R = B \cdot r_{gyro}$) of 1.8 and 3 TV for protons and helium respectively. Both of these spectra are best described by a broken power-law, with the break around $R \sim 300$ GV. The most important collision cross sections for the antiproton production are the following including their contribution to the total antiproton production: $\sigma_{p,H \rightarrow \bar{p}}$ (60-65%), $\sigma_{p,He \rightarrow \bar{p}}$, $\sigma_{He,H \rightarrow \bar{p}}$ (together 32-37%) and $\sigma_{He,He \rightarrow \bar{p}}$ (< 3%). Taking into account all the uncertainties on these cross sections, we find the uncertainty band for the astrophysical \bar{p}/p ratio, as shown in the red uncertainty band of figure 24. By semi-analytically solving the full transport equation for charged particles in 2D cylindrical halo model of

the Galaxy, the propagation of the antiprotons through the Galaxy is simulated. In these simulations \bar{p} annihilation, energy losses, "tertiary production" and diffusive reacceleration are taken into account. The yellow uncertainty band of figure 24 shows the impact of the propagation onto the uncertainty. The MIN, MED and MAX lines show different sets of diffusion parameters that minimize or maximize the hypothetical primary, dark matter antiproton flux at Earth. Details of this transport simulation can be found in [100]. Finally antiprotons that want to reach Earth have to penetrate the heliosphere, where they are subject to Solar modulation. To reach Earth, the antiprotons have to work against the Solar magnetic field that shields the Earth from low energy particles. This causes the antiprotons to lose energy. The solar modulation makes that we are unsure about the size of this effect, which plays a bigger role for low energy particles than for high energy particles. The solar modulation is parameterized by the Fisk potential, ϕ_F . This effect is summarized in the green uncertainty band of figure 24.

4.2.2 Antiproton dark matter constraints

As said before, figure 24 shows the predicted secondary \bar{p}/p ratio, overplotted with the PAMELA [101] and AMS-02 [98] data. The fiducial curve assumes the reference values for the different contributions to the uncertainties. The coloured bands represent the different uncertainties as discussed in the section above. From figure 24 it is clear that there is no antiproton excess that can be identified with respect to the background, and thus there is no real need for primary sources. This also means that there is limited room left for a dark matter antiproton component.

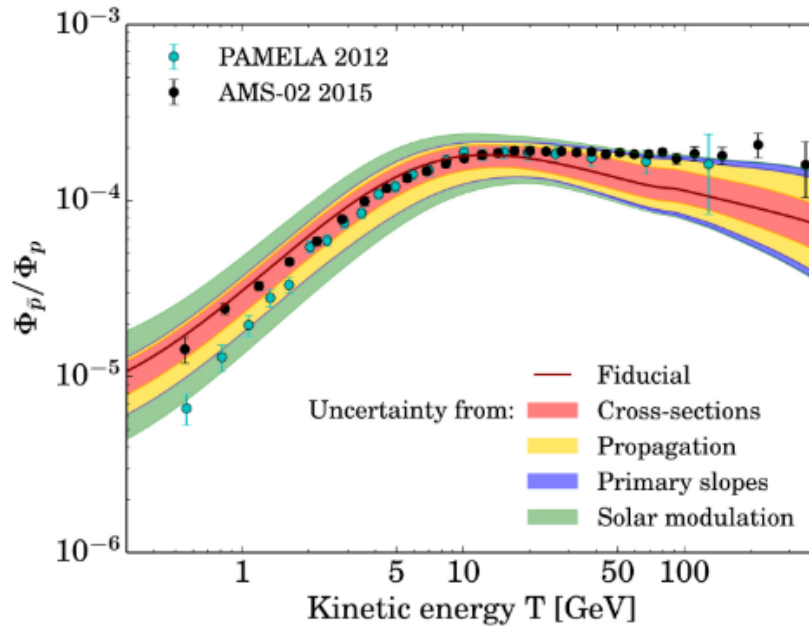


Figure 24: Figure from [102] (partly based on figure 8 of [101]): The combined total uncertainty on the predicted secondary \bar{p}/p ratio, superimposed to the older Pamela data [99] and the new Ams-02 data [98]. The curve labelled 'fiducial' assumes the reference values for the different contributions to the uncertainties: best fit proton and helium fluxes, central values for the cross sections, Med propagation and central value for the Fisk potential. The colored bands represent the individual uncertainties on the input proton and helium fluxes (blue), \bar{p} production cross sections in the interstellar medium (red), Galactic propagation (yellow) and Solar modulation (green).

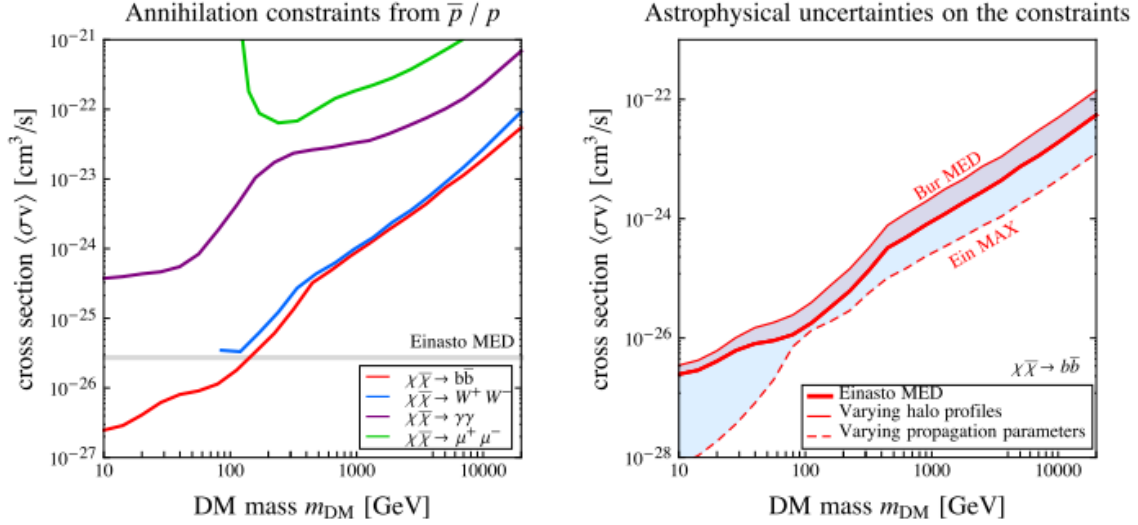


Figure 25: Figure from [102]: Annihilating dark matter: constraints based on AMS-02 data [98]. Left Panel: current constraints from the antiproton to proton ratio for different annihilation channels. The areas above the curves are excluded. Right Panel: illustration of the impact of dark matter-related astrophysical uncertainties: the constraint for the $\bar{b}b$ channel spans the shaded band when varying the propagation parameters (dashed lines) or the halo profiles (solid lines).

To put constraints on the dark matter annihilation using the AMS-02 data following [102] four primary annihilation channels are considered: $\chi\chi \rightarrow b\bar{b}$, $\chi\chi \rightarrow W^+W^-$, $\chi\chi \rightarrow \mu^+\mu^-$ and $\chi\chi \rightarrow \gamma\gamma$. All of these products decay into antiprotons (and other particles). Using the recipe from [104] the maximum dark matter contributions to the antiproton - proton ratio are calculated for three different propagation models (MIN, MED and MAX). These are the sets of propagation parameters that minimize or maximize the dark matter antiproton flux at Earth. Fixing the propagation model to either of these, for a given dark matter mass and cross sections, the dark matter antiproton flux is added to the background: $\phi_{tot}(m_{DM}, <\sigma v>, A, \phi_F) = \phi_{background}(A, \phi_F) + \phi_{DM}(m_{DM}, <\sigma v>, \phi_F)$, where the best fit amplitude, A , and Fick potential, ϕ_F , are implemented. By solving $\chi^2_{DM}(m_{DM}, <\sigma v>, A, \phi_F) - \chi^2_0 = 4$ (where χ^2_0 is the minimum chi-squared of the background-only case) for $<\sigma v>$ and thereby obtain an exclusion contour. This calculation is made for each dark matter mass. Also two dark matter density profiles, Einasto and Burkert, are considered. In the results of this calculation only the propagation schemes that provide a decent explanation of the background (MAX and MED) are taken into account.

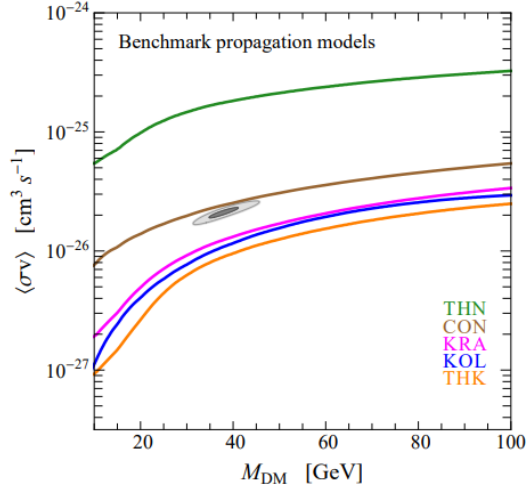


Figure 26: Figure from [103]: 3σ exclusion contours on $\langle\sigma v\rangle$ for 100% dark matter annihilation into $b\bar{b}$. The Fick potential for the antiprotons is taken to be the Fick potential for protons: $\phi_F^p = \phi_F^p \pm 50\%$. The different lines show different propagation set-ups. The gray area is the best-fit region identified for the claimed dark matter gamma-ray detection in [1].

The resulting constraints on the cross section and mass are shown in figure 25. The left panels show the constraints from the antiproton to proton ratio for different annihilation channels but for fixed dark matter density profile (Einasto) and propagation parameters (MED). The areas above each of these lines are the cross section and mass regions that are excluded by these measurements. It is clear that the $\bar{b}b$ channel gives the strongest constraints, and the $\mu^+\mu^-$ and $\gamma\gamma$ channel the weakest. The latter is not surprising, since we don't expect any antiprotons from a leptonic channel. The only antiproton contribution from this channel is via electroweak bremsstrahlung [105, 106]. The right panel illustrates the impact of the astrophysical uncertainties for the $\bar{b}b$ channel. The dark matter density profile and propagation parameters give rise to the uncertainty band.

From the left panel of figure 25 it is clear that the limits on the cross section for the $\bar{b}b$ channel are the strongest and even exclude the thermal relic cross section at energies lower than ~ 100 GeV. The $\mu^+\mu^-$ and $\gamma\gamma$ channels are orders of magnitude weaker and don't provide very useful constraints. The right panel shows the difficulties in constraining the dark matter cross section via antiprotons, since the uncertainties in halo profile and propagation effects give rise to order of magnitude uncertainty bands.

Figure 26 shows similar constraints to figure 25 using the antiproton fluxes from PAMELA [99] to explain the gamma-ray excess that was linked to dark matter by [1]. They show 3σ exclusion contours on $\langle \sigma v \rangle$ for 100% dark matter annihilation into $\bar{b}b$. The Fick potential for the antiprotons is taken to be the Fick potential for protons: $\phi_F^{\bar{p}} = \phi_F^p \pm 50\%$. The different lines show different propagation set-ups. The thin propagation model (green) for example implies a thin dark matter halo. This means that antiprotons created in the galactic center are not able to scatter to Earth, therefore the observed flux is low and the constraints on the dark matter cross section weak. The thick propagation model (yellow) for example imposes a thick dark matter halo. This means that antiprotons created in the galactic center are able to scatter to Earth, therefore the observed flux is high and the constraints on the dark matter cross section are strong. The gray area is the best-fit region identified for the claimed dark matter gamma-ray detection in [1]. To find an agreement between the gamma-ray and antiproton data we have to exclude the THK, KOL and KRA halo profile models. These three models exclude the cross section and mass combination as found by [1]. The other two halo models, THN and CON, lie above the gray area and therefore it is possible that this claimed gamma-ray dark matter annihilation detection agrees with one of these models. We can not make any strong claims about whether the gray area represents a real detection (of the gamma-rays of dark matter annihilation), but we can conclude that there is tension between this claim and the antiproton models.

4.3 Anti-nucleus channel - (Paul)

A different approach of detecting dark matter would be to measure the flux of anti-nuclei, which consist of anti-nucleons that originate from dark matter annihilation processes. Specifically the anti-deuteron (\bar{d}) and anti-helium ($\bar{^3He}$) flux, which could give compelling hints towards dark matter. Although such a signal has already been proposed over a decade ago, it has not been measured yet. Because of the high energy threshold of creating either one of the anti-nuclei, a large suppression is expected on the background signal at low kinetic energies, at the expense of having an extremely low flux signal. In the context of indirect dark matter searches, it is therefore important to simulate the anti-nucleus flux that we can expect detectors to measure.

4.3.1 Anti-nuclei production

For the production of both the \bar{d} and $\bar{^3He}$ nuclei, antiprotons and antineutrons need to coalesce. This process can be described by the coalescence model, see formula 29, which comes from relating the

probability of finding a antineutron and antiproton within p_0 distance in momentum space, assuming equal production cross sections and momentum distributions [107].

$$\gamma \frac{d^3 N_{\bar{A}}}{d\vec{p}_{\bar{A}}^3} = \left(\frac{4\pi}{3} p_0^3\right)^{(A-1)} \left(\gamma \frac{d^3 N_{\bar{p}}}{d\vec{p}_{\bar{p}}^3}\right)^A \quad (29)$$

Where A stands for the mass number of the nucleus, γ for the Lorentz factor and where the \bar{p} spectrum has been normalized per annihilation event, see formula 30. The coalescence momentum p_0 , is the effective momentum limit for which two nucleons will coalesce. This parameter, although extremely important for the spectrum, is unfortunately not well understood as we'll see in section 4.3.2. Filling in $A = 2$ for \bar{d} and $A = 3$ for $\bar{^3He}$, shows a dependence of $\propto p_0^3$ and $\propto p_0^6$ respectively, which is one of the major caveats of this method. It should also be noted that, as one would expect, increasing the mass number A will result in a suppression factor for the anti nuclei yield, since typically $p_0 \sim 0.2$. It is therefore helpful to look at \bar{d} and $\bar{^3He}$, increasing the mass number will result in a decrease in coalescence of a estimated factor $O(10^{-4})$, where knowledge on the \bar{p} spectrum is assumed.

$$\frac{d^3 N_{\bar{p}}}{d\vec{p}_{\bar{p}}^3} = \frac{1}{\sigma_R} \frac{d^3 \sigma_{\bar{p}}}{d\vec{p}_{\bar{p}}^3} \quad (30)$$

Formula 30 shows the particle momentum spectrum, in which σ_R is the total nucleon-nucleus reaction cross section and where constraints on the cross section $\sigma_{\bar{p}}$ can be found in section 4.2.2.

4.3.2 Coalescence momentum p_0

As mentioned before, the momentum spectrum has a large dependence on coalescence momentum p_0 . Since there is little experimental data on anti-nuclei, a similar production has been used to determine p_0 , i.e. $e^+ + e^- \rightarrow \bar{d}$. Measurements by ALEPH on the \bar{d} production rates through said process have been found to be $R_{\bar{d}} = (5.9 \pm 1.8 \pm 0.5) \times 10^{-6}$ anti-deuterons per Z-boson decay for momentum $\vec{p}_{\bar{d}} = (0.62, 1.03) GeV$, as shown in figure 27 (green line). Also depicted in this figure are three different models that calculate the production rate as a function of the coalescence momentum p_0 :

- **Old Model**; in which uncorrelated production of $\bar{p}\bar{n}$ is assumed [108].
- **MC(Δp)**; Monte Carlo model in which the relative momentum of the $\bar{p}\bar{n}$ pair is cut off.
- **MC($\Delta p + \Delta r$)**; in which the previous model is extended to also include a cut off for the physical distance of the $\bar{p}\bar{n}$ pair.

It should be noted that determination of p_0 through Z-boson decay does not resemble any particular dark matter candidate, but is rather done out of necessity since there is not much literature on this parameter. However, for light anti-nuclei (i.e. $A \leq 4$), consistent results have been found in case of astrophysical spallations between \bar{d} and $\bar{^3He}$ while using the same coalescence momentum p_0 . Secondly, it is assumed that the coalescence momentum p_0 is constant. Imagining an energy dependence on this parameter would change the anti-nuclei spectrum drastically, but since this is not tested, the assumption could be valid. Looking at the measurement by ALEPH (i.e. $R_{\bar{d}} = (5.9 \pm 1.8 \pm 0.5) \times 10^{-6}$), we find the 1σ significance results to be:

- **Old Model** $\rightarrow p_0 = 160 \pm 19 MeV$
- **MC(Δp)** $\rightarrow p_0 = 180 \pm 18 MeV$
- **MC($\Delta p + \Delta r$)** $\rightarrow p_0 = 195 \pm 22 MeV$.

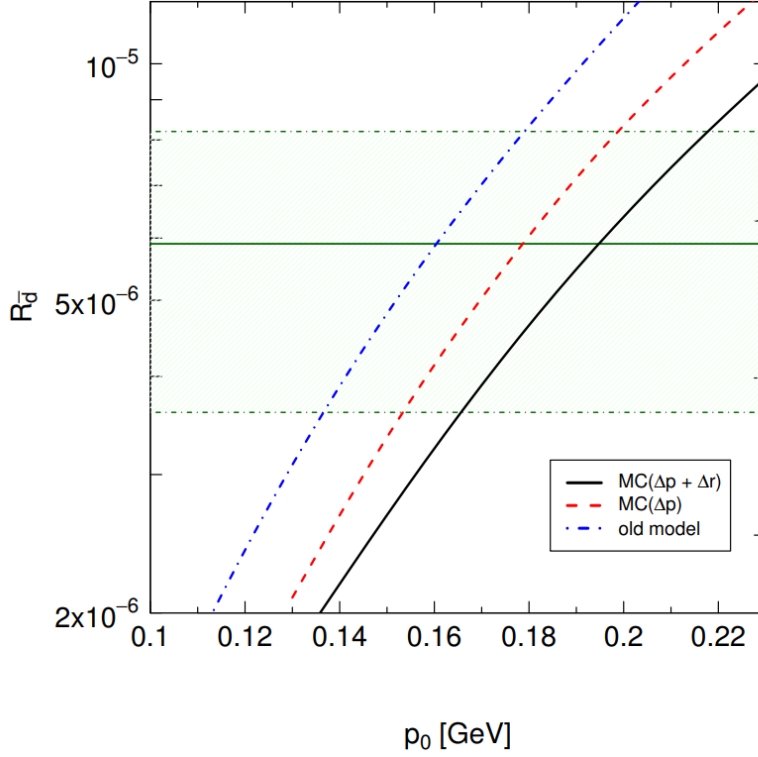


Figure 27: Figure from [109]: Production rate of anti-deuterons \bar{d} from $e^+ + e^- \rightarrow \bar{d}$ at Z resonance as a function of coalescence momentum p_0 for three different models. The green line denotes the measurement by ALEPH.

Because the coalescence spectrum heavily depends on this value (i.e. to the power 3–6, see section 4.3.1), the differences between model results become quite large, especially when looking at their uncertainties. Continuing our report on the \bar{d} and ${}^3\overline{He}$ flux simulation, the coalescence momentum value of $p_0 = 195 \text{ MeV}$ will be used [109].

4.3.3 Propagation through the galactic medium

After anti-nuclei have been produced, some of them will propagate through the galactic medium towards a detector at the top of earth atmosphere. Their number density $f(t, \vec{x}, T) = dN_{\bar{d}, \overline{He}}/dT$ per unit of kinetic energy T can then be described by formula 31, for which we closely followed [110] and [109].

$$\frac{\partial f}{\partial t} - K(T) \cdot \nabla^2 f + \frac{\partial}{\partial z}(\text{sign}(z)fV_c) = Q - 2h\delta(z)\Gamma f \quad (31)$$

In this transport equation, $K(T)$ is the diffusion coefficient through the medium, V_c is the convective velocity of galactic wind and Q is the dark matter annihilation source term, which we have seen before in equation 1, but now for a anti-nucleon spectrum. The last term describes interactions with the inter stellar medium (ISM), which is dependent upon: Γ the annihilation rate of \bar{d} and \overline{He} (due to ISM interactions), $\delta(z)$ which refers to the galactic plane and h which depicts its height. This equation is then optimized and solved inside a cylindrical volume $z = \pm L$ and $r = 20 \text{ kpc}$. Table 28 shows a categorization (i.e. MIN, MED and MAX) of these parameters by [111], in which MED corresponds to the most likely scenario, and MIN/ MAX to its uncertainty band.

Model	Galactic charged CR propagation parameters			
	δ	\mathcal{K}_0 [kpc ² /Myr]	V_{conv} [km/s]	L [kpc]
MIN	0.85	0.0016	13.5	1
MED	0.70	0.0112	12	4
MAX	0.46	0.0765	5	15

Figure 28: Table from [110] by [111]: Propagation parameters in galactic medium

4.3.4 Propagation through the heliosphere

The last effects that have to be considered are those of heliosphere propagation, in which the cosmic rays lose their energy because of the solar wind. Solar modulations are a very dynamical and challenging problem by itself, and depends on properties like solar intensity and orientation of its magnetic field, both of which change regularly. Propagation of the cosmic ray phase space density f can be described by equation 32 from [109].

$$\frac{\partial f}{\partial t} = -(\vec{V}_{sw} + \vec{v}_d) \cdot \nabla f + \nabla \cdot (K \cdot \nabla f) + \frac{P}{3} (\nabla \cdot \vec{V}_{sw}) \frac{\partial f}{\partial P} \quad (32)$$

In which K is the diffusion tensor, \vec{V}_{sw} is the solar wind speed, \vec{v}_d the drift velocity, and P the momentum of the cosmic ray. A detailed explanation of anti-nuclei propagating through the heliosphere is presented in [109]. In this simulation, heliosphere propagation parameters were used that minimize the effect of solar modulations, i.e. equation 32.

4.3.5 Flux predictions

Considering both of the propagation transport equations and the anti-nuclei coalescence spectrum, the following results can be found for the expected anti-nuclei flux at the top of earths atmosphere via dark matter annihilation as a function of their kinetic energy; figure 30 in the case of anti-deuteron \bar{d} and figure 29 in the case of the anti-Helium ${}^3\bar{He}$. There are three annihilation channels depicted (although slightly different dark matter masses were used); light dark matter mass in the $u\bar{u}$ channel ($m_{DM} = 10 - 20 GeV$) on the left, medium dark matter mass in the $b\bar{b}$ channel ($m_{DM} = 20 - 40 GeV$) in the middle and lastly heavy dark matter mass in the W^+W^- channel ($m_{DM} = 1 TeV$) on the right. This variety in masses cover the typical WIMP scale range from light quarks up to gauge bosons, other channels depict quite similar fluxes compared to these. For both anti-nuclei, a Einasto dark matter density profile was assumed (equation 2.2.2).

The red bands in figure 29 show the predicted anti-helium flux, in which MIN/MED/MAX denote the propagation parameters used (table 28). Measurements from PAMELA constrain the amount of anti-protons which are produced in dark matter annihilation (see section 4.2.2). This is depicted in dark red as in agreement with measurements and in light red as excluded. The blue lines denote the cosmic background anti-helium noise. For low to medium WIMP scale masses the background flux spectrum peaks at higher energy, due to the large energy threshold ($\sim 31m_p$) of creating anti-helium from spallation of cosmic rays on the inter stellar gas. The fact that the background is nicely separated from the anti-nucleus signal is a promising feature of this dark matter detection method. The grey areas describe constraints from anti-helium / helium ratio measurements (by AMS-01, BESS and PAMELA), which can be converted to anti-helium flux by multiplying by a measured helium flux. The expected probe region of AMS-02 is shown in green, which unfortunately does not have the sensitivity to probe this dark matter signature. Even for very optimistic values of p_0 , AMS-02 sensitivity fall a few orders of magnitude short. With this comes the major downside of this method, namely that it is challenging to measure the typical ratio of anti-nuclei / nuclei $\sim 10^{-13}$, which is extremely low.

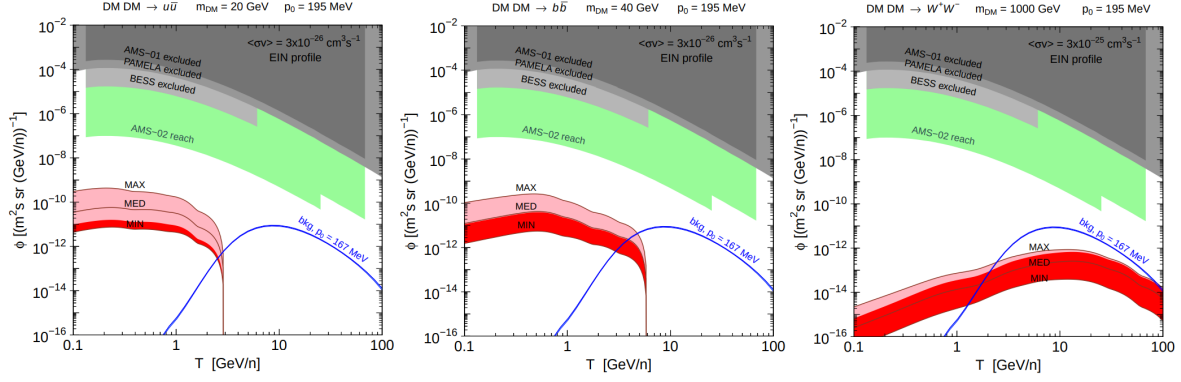


Figure 29: Figure from [110]: Anti-helium flux prediction from dark matter annihilation as a function of their kinetic energy. The left panel considers a 20GeV dark matter particle ($u\bar{u}$ channel), the middle panel a 40GeV dark matter particle ($b\bar{b}$ channel), and the right panel a 1TeV dark matter particle (W^+W^- channel). In red the flux predictions (MIN/MED/MAX) at the top of earth's atmosphere. The background, for which $p_0 = 165\text{MeV}$ is assumed, is depicted by the blue line. Several constraints are shown as the grey area, as well as the future expectations of AMS-02, in green.

Anti-deuteron flux predictions on the other hand are much more promising, because the dark matter signal can just be probed by experiments that are currently in development (GAPS LSB+ and AMS-02), as shown by the grey and orange areas in figure 30. The black line depicts the background anti-deuteron noise, that also shows good separation from the anti-deuteron flux signal which is depicted by the blue, green and red line for MED parameters (table 28). The different colours represent different parameters used for the solar modulations, for which the difference in flux stays mostly within a reasonable factor. The flux predictions are much higher compared to anti-helium because of the lower mass number $A = 2$ in this case, instead of $A = 3$ for anti-helium in equation 29. In other words, its easier for the anti-nucleons to coalesce towards anti-deuteron than towards anti-helium. In both the anti-helium and anti-deuteron case we find the expected flux signal to shift within the region of the noise, for large WIMP mass $m_{DM} \sim 1\text{TeV}$. Meaning that this method of dark matter detection is only sensible in the WIMP mass region of $m_{DM} \sim O(\text{GeV})$.

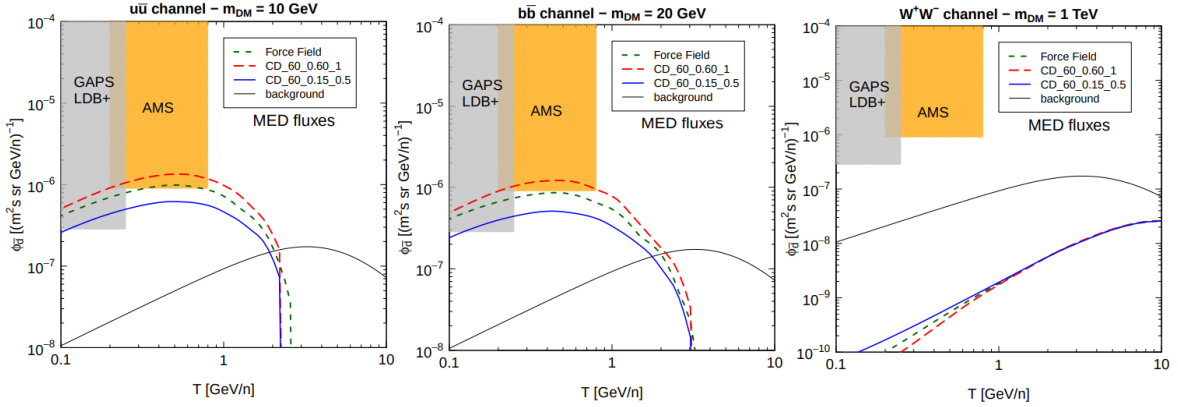


Figure 30: Figure from [109]: Anti-deuteron flux prediction from dark matter annihilation as a function of their kinetic energy. The left panel considers a 10GeV dark matter particle ($u\bar{u}$ channel), the middle panel a 20GeV dark matter particle ($b\bar{b}$ channel) and the right panel a 1TeV dark matter particle (W^+W^- channel). The three coloured curves denote the expected flux in which different solar modulation models were used, for MED parameters. The background from secondary production is denoted as the black line. In grey the expected sensitivity for GAPS LDB+ and in orange those of AMS-02

5 Summary - (Iris & Paul)

Figure 31 from [112] shows a summary of the current indirect detection experimental constraints on the dark matter cross section and mass. The constraints are for the annihilation to b-quark pairs. The gray band shows the thermal relic cross section. The indirect detection methods using gamma-rays (Fermi-LAT) and cosmic rays (AMS) show the best constraints in the lower energy region of the figure, while the air Cherenkov telescopes (H.E.S.S.) are driving the present limits at higher energies. The CMB limits do not lead in sensitivity at the moment but are an important check for any claims of dark matter annihilation detections. The Icecube and ANTARES results are neutrino detectors and aren't discussed in this review. At present times the neutrino limits can not compete with the indirect detection measurements we discussed.

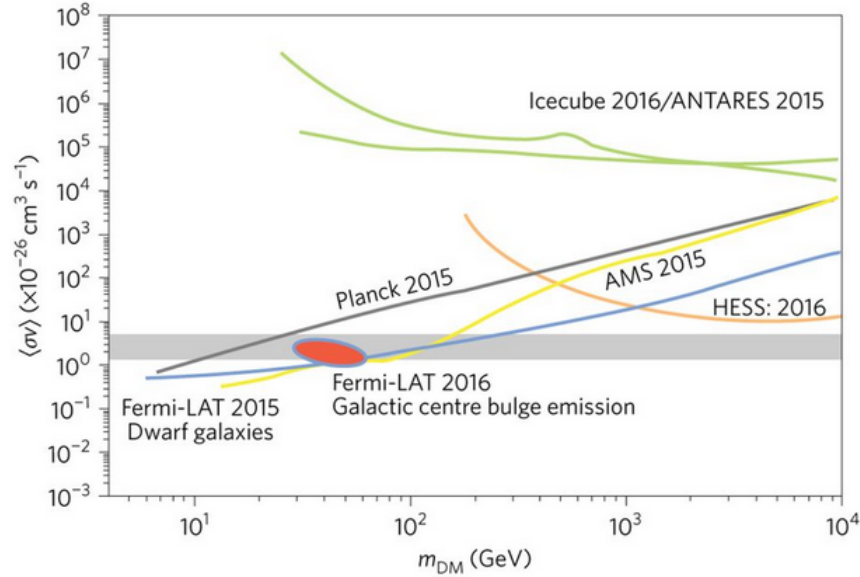


Figure 31: Figure from [112]: Constraints on the dark matter mass and cross section for the annihilation to b-quark pairs. Indirect methods exploring gamma-ray photons and cosmic rays from satellite measurements compete well up to hundreds of GeVs, at higher energies, air Cherenkov telescopes appear to be driving the present limits. The thermal relic cross section is indicated by the light grey band. Note that different assumptions for the dark matter distributions affect these limits quantitatively, but do not change the situation qualitatively. Data taken from [41],[37],[102],[74],[113],[114],[115],[1],[116].

From figure 31 we see that current limits start to constrain the canonical thermal relic annihilation cross section for WIMP dark matter. As the sensitivity of future experiments such as the CTA are expected to increase by an order of magnitude, it is clear that in the next several years indirect detection methods enter exciting times. Next to the gamma-ray experiments also the anti-nucleus channels for indirect detection prove promising. One of the major advantages of the latter method, is the clear separation between the cosmic noise and the dark matter annihilation signal for $m_{DM} \sim O(GeV)$. This shift in flux spectrum is caused by the high energy threshold of creating anti-nuclei. The only downside being, a very small expected flux. From simulations it has become clear that the anti-deuteron flux, with mass number $A = 2$, lies just within the region of the future detectors (GAPS LDB+ and AMS) sensitivity. Unfortunately, future prospect for the anti-helium channel detectors fall a few orders of magnitude short in their sensitivity. Having said so, the clear separation of both signals depicted in figures 29 and 30 could be playing a major role in future dark matter searches.

Finally we can always check claims of dark matter detections against the well-known CMB power spectrum, to see whether or not this allows for the claimed detection.

Although claims of detections have been made in the past few years ([1] and [2]), sensitive indirect searches in multiple targets as well as multi-messenger searches will be required to validate or reject them. In the upcoming years the indirect detection experiments enter an exciting era where hopefully dark matter annihilation will be detected and the fundamental properties of this mysterious particle will be pinned down.

6 Appendix

6.1 Appendix A: Lunar assisted trajectory

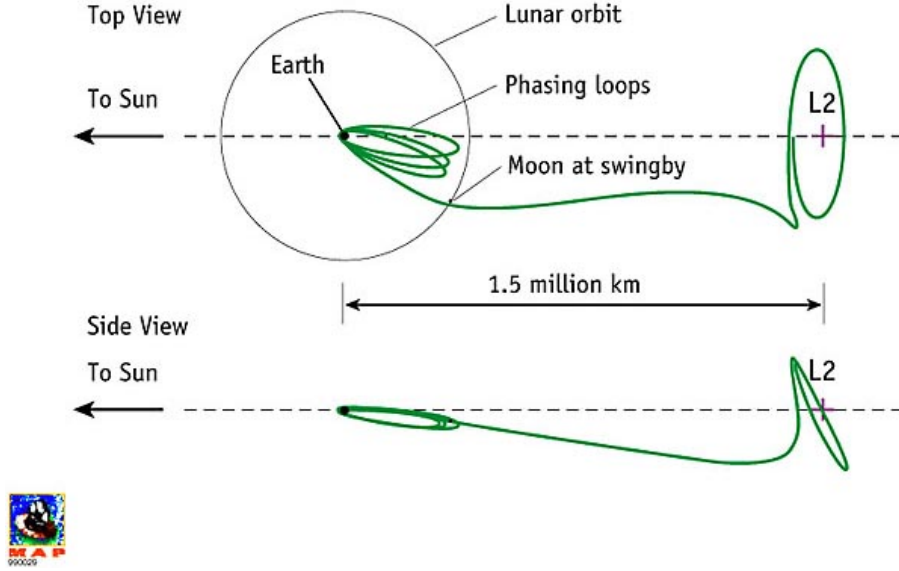


Figure 32: Figure from NASA website. WMAP lunar assisted trajectory to the Sun-Earth L2 libration point.

6.2 Appendix B: Jupyter notebook

The Jupyter notebook named `J_factors.ipynb` can be used to experiment with and calculate the J-factors of different dwarf galaxies and galaxy clusters. The calculation of the J-factors is described in section 2.1 in equation 4. The input parameters are described in the code and can be used to plot the J-factor and/or D-factor of the Milky Way, blabla clusters. If there was any observational data available, this is overplotted.

The J-factor data for the dwarf galaxies is taken from [117], the Milky way data is from [118]. To calculate the scale radii we used 5 times the half-radii as described in [119]. The central density for the dwarf galaxies was calculated using the relation between central density and scale radius as described by Burkert: [120]

$$\rho_0 = 2.7 \cdot 10^{-2} \left(\frac{r_s}{kpc} \right)^{-2/3} \frac{M_\odot}{pc^3} \quad (33)$$

This density was afterwards converted to the right units (GeV/cm^3).

Input parameters for the galaxy clusters, such as the central density and scale radius are taken from [14, 15, 16]. For more information on the interplay between the input from this papers, see the script.

References

- [1] Tansu Daylan, Douglas P Finkbeiner, Dan Hooper, Tim Linden, Stephen KN Portillo, Nicholas L Rodd, and Tracy R Slatyer. The characterization of the gamma-ray signal from the central milky way: A case for annihilating dark matter. *Physics of the Dark Universe*, 12:1–23, 2016.
- [2] Richard Bartels, Suraj Krishnamurthy, and Christoph Weniger. Strong support for the millisecond pulsar origin of the galactic center gev excess. *Physical Review Letters*, 116(5):051102, 2016.
- [3] T. M. Nieuwenhuizen. Subjecting dark matter candidates to the cluster test. *ArXiv e-prints*, October 2017.
- [4] A. Bottino, V. de Alfaro, N. Fornengo, G. Mignola, and S. Scopel. On the neutralino as dark matter candidate. II. Direct detection. *Astroparticle Physics*, 2:77–90, February 1994.
- [5] J Carr, G Lamanna, and J Lavalle. Indirect detection of dark matter. *Reports on Progress in Physics*, 69(8):2475, 2006.
- [6] Jennifer M. Gaskins. A review of indirect searches for particle dark matter. *Contemporary Physics*, 57(4):496–525, 2016.
- [7] Torbjörn Sjöstrand, Patrik Eden, Christer Friberg, Leif Lönnblad, Gabriela Miu, Stephen Mrenna, and Emanuel Norrbin. High-energy-physics event generation with pythia 6.1. *Computer Physics Communications*, 135(2):238–259, 2001.
- [8] Gennaro Corcella, Ian G Knowles, Giuseppe Marchesini, Stefano Moretti, Kosuke Odagiri, Peter Richardson, Michael H Seymour, and Bryan R Webber. Herwig 6: an event generator for hadron emission reactions with interfering gluons (including supersymmetric processes). *Journal of High Energy Physics*, 2001(01):010, 2001.
- [9] Argyro Tasitsiomi and Angela V Olinto. Detectability of neutralino clumps via atmospheric cherenkov telescopes. *Physical Review D*, 66(8):083006, 2002.
- [10] Gianfranco Bertone, Geraldine Servant, and Guenter Sigl. Indirect detection of kaluza-klein dark matter. *Physical Review D*, 68(4):044008, 2003.
- [11] S. Profumo. TASI 2012 Lectures on Astrophysical Probes of Dark Matter. *ArXiv e-prints*, January 2013.
- [12] G. Steigman, B. Dasgupta, and J. F. Beacom. Precise relic WIMP abundance and its impact on searches for dark matter annihilation. *Physical Review*, 86(2):023506, July 2012.
- [13] Marco Cirelli, Gennaro Corcella, Andi Hektor, Gert Hütsi, Mario Kadastik, Paolo Panci, Martti Raidal, Filippo Sala, and Alessandro Strumia. Pppc 4 dm id: a poor particle physicist cookbook for dark matter indirect detection. *Journal of Cosmology and Astroparticle Physics*, 2011(03):051, 2011.
- [14] Andi Hektor, Martti Raidal, and Elmo Tempel. Evidence for indirect detection of dark matter from galaxy clusters in fermi γ -ray data. *The Astrophysical Journal Letters*, 762(2):L22, 2012.
- [15] Kimberly K Boddy, Jason Kumar, and Louis E Strigari. The effective j-factor of the galactic center for velocity-dependent dark matter annihilation. *arXiv preprint arXiv:1805.08379*, 2018.
- [16] Emma Storm, Tesla E Jeltama, Stefano Profumo, and Lawrence Rudnick. Constraints on dark matter annihilation in clusters of galaxies from diffuse radio emission. *The Astrophysical Journal*, 768(2):106, 2013.

- [17] A. Abramowski, F. Aharonian, F. Ait Benkhali, A. G. Akhperjanian, E. Angüner, M. Backes, S. Balenderan, A. Balzer, A. Barnacka, Y. Becherini, and et al. Search for dark matter annihilation signatures in H.E.S.S. observations of dwarf spheroidal galaxies. *Physical Review*, 90(11):112012, December 2014.
- [18] Fabio Iocco, Miguel Pato, Gianfranco Bertone, and Philippe Jetzer. Dark matter distribution in the milky way: microlensing and dynamical constraints. *Journal of Cosmology and Astroparticle Physics*, 2011(11):029, 2011.
- [19] Frank C. van den Bosch and Rob A. Swaters. Dwarf galaxy rotation curves and the core problem of dark matter haloes. *Monthly Notices of the Royal Astronomical Society*, 325(3):1017–1038, 2001.
- [20] J. Diemand, M. Kuhlen, P. Madau, M. Zemp, B. Moore, D. Potter, and J. Stadel. Clumps and streams in the local dark matter distribution. *Nature*, 454:735–738, August 2008.
- [21] Mattia Fornasa and Anne M Green. Self-consistent phase-space distribution function for the anisotropic dark matter halo of the milky way. *Physical Review D*, 89(6):063531, 2014.
- [22] Paolo Gondolo and Joseph Silk. Dark matter annihilation at the galactic center. *Physical Review Letters*, 83(9):1719, 1999.
- [23] Oleg Y Gnedin, Andrey V Kravtsov, Anatoly A Klypin, and Daisuke Nagai. Response of dark matter halos to condensation of baryons: cosmological simulations and improved adiabatic contraction model. *The Astrophysical Journal*, 616(1):16, 2004.
- [24] Oleg Y Gnedin, Daniel Ceverino, Nickolay Y Gnedin, Anatoly A Klypin, Andrey V Kravtsov, Robyn Levine, Daisuke Nagai, and Gustavo Yepes. Halo contraction effect in hydrodynamic simulations of galaxy formation. *arXiv preprint arXiv:1108.5736*, 2011.
- [25] B. Moore, T. Quinn, F. Governato, J. Stadel, and G. Lake. Cold collapse and the core catastrophe. *Monthly Notices of the Royal Astronomical Society*, 310:1147–1152, December 1999.
- [26] J. J. Adams, J. D. Simon, M. H. Fabricius, R. C. E. van den Bosch, J. C. Barentine, R. Bender, K. Gebhardt, G. J. Hill, J. D. Murphy, R. A. Swaters, J. Thomas, and G. van de Ven. Dwarf Galaxy Dark Matter Density Profiles Inferred from Stellar and Gas Kinematics. *The astrophysical journal*, 789:63, July 2014.
- [27] J. F. Navarro, E. Hayashi, C. Power, A. R. Jenkins, C. S. Frenk, S. D. M. White, V. Springel, J. Stadel, and T. R. Quinn. The inner structure of Λ CDM haloes - III. Universality and asymptotic slopes. *Monthly Notices of the Royal Astronomical Society*, 349:1039–1051, April 2004.
- [28] Liang Gao, Julio F Navarro, Shaun Cole, Carlos S Frenk, Simon DM White, Volker Springel, Adrian Jenkins, and Angelo F Neto. The redshift dependence of the structure of massive λ cold dark matter haloes. *Monthly Notices of the Royal Astronomical Society*, 387(2):536–544, 2008.
- [29] J. F. Navarro, A. Ludlow, V. Springel, J. Wang, M. Vogelsberger, S. D. M. White, A. Jenkins, C. S. Frenk, and A. Helmi. The diversity and similarity of simulated cold dark matter haloes. *Monthly Notices of the Royal Astronomical Society*, 402:21–34, February 2010.
- [30] J. Einasto. On the Construction of a Composite Model for the Galaxy and on the Determination of the System of Galactic Parameters. *Trudy Astrofizicheskogo Instituta Alma-Ata*, 5:87–100, 1965.
- [31] RA Swaters, BF Madore, Frank C van den Bosch, and M Balcells. The central mass distribution in dwarf and low surface brightness galaxies. *The Astrophysical Journal*, 583(2):732, 2003.

- [32] Kristine Spekkens, Riccardo Giovanelli, and Martha P. Haynes. The Cusp/Core Problem in Galactic Halos: Long-Slit Spectra for a Large Dwarf Galaxy Sample. *The Astronomical Journal*, 129(5):2119–2137, may 2005.
- [33] Gianfranco Bertone, Andrew R Zentner, and Joseph Silk. New signature of dark matter annihilations: Gamma rays from intermediate-mass black holes. *Physical Review D*, 72(10):103517, 2005.
- [34] WB Atwood, Aous A Abdo, Markus Ackermann, W Althouse, B Anderson, M Axelsson, L Baldini, J Ballet, DL Band, Guido Barbiellini, et al. The large area telescope on the fermi gamma-ray space telescope mission. *The Astrophysical Journal*, 697(2):1071, 2009.
- [35] Markus Ackermann, Marco Ajello, WB Atwood, Luca Baldini, Guido Barbiellini, D Bastieri, K Bechtol, R Bellazzini, RD Blandford, ED Bloom, et al. Constraints on the galactic halo dark matter from fermi-lat diffuse measurements. *The Astrophysical Journal*, 761(2):91, 2012.
- [36] Andrea Albert, Brandon Anderson, Keith Bechtol, Alex Drlica-Wagner, Manuel Meyer, Miguel Sánchez-Conde, L Strigari, M Wood, TMC Abbott, Filipe B Abdalla, et al. Searching for dark matter annihilation in recently discovered milky way satellites with fermi-lat. *The Astrophysical Journal*, 834(2):110, 2017.
- [37] M Ackermann, A Albert, Brandon Anderson, WB Atwood, L Baldini, G Barbiellini, D Bastieri, K Bechtol, R Bellazzini, E Bissaldi, et al. Searching for dark matter annihilation from milky way dwarf spheroidal galaxies with six years of fermi large area telescope data. *Physical Review Letters*, 115(23):231301, 2015.
- [38] Gary Steigman, Basudeb Dasgupta, and John F Beacom. Precise relic wimp abundance and its impact on searches for dark matter annihilation. *Physical Review D*, 86(2):023506, 2012.
- [39] Felix Aharonian, AG Akhperjanian, AR Bazer-Bachi, M Beilicke, Wystan Benbow, David Berge, K Bernlöhr, C Boisson, Oliver Bolz, V Borrel, et al. Hess observations of the galactic center region and their possible dark matter interpretation. *Physical Review Letters*, 97(22):221102, 2006.
- [40] A Abramowski, Fabio Acero, F Aharonian, AG Akhperjanian, G Anton, A Barnacka, U Barres De Almeida, AR Bazer-Bachi, Yvonne Becherini, J Becker, et al. Search for a dark matter annihilation signal from the galactic center halo with hess. *Physical Review Letters*, 106(16):161301, 2011.
- [41] H. Abdallah et al. Search for γ -Ray Line Signals from Dark Matter Annihilations in the Inner Galactic Halo from 10 Years of Observations with H.E.S.S. *Phys. Rev. Lett.*, 120(20):201101, 2018.
- [42] S Archambault, A Archer, W Benbow, R Bird, E Bourbeau, T Brantseg, M Buchovecky, JH Buckley, V Bugaev, K Byrum, et al. Dark matter constraints from a joint analysis of dwarf spheroidal galaxy observations with veritas. *Physical Review D*, 95(8):082001, 2017.
- [43] Max L Ahnen, S Ansoldi, LA Antonelli, C Arcaro, D Baack, A Babić, B Banerjee, P Bangale, U Barres de Almeida, JA Barrio, et al. Indirect dark matter searches in the dwarf satellite galaxy ura major ii with the magic telescopes. *Journal of Cosmology and Astroparticle Physics*, 2018(03):009, 2018.
- [44] AU Abeysekara, A Albert, R Alfaro, C Alvarez, R Arceo, JC Arteaga-Velázquez, D Avila Rojas, HA Ayala Solares, A Becerril, E Belmont-Moreno, et al. A search for dark matter in the galactic halo with hawc. *Journal of Cosmology and Astroparticle Physics*, 2018(02):049, 2018.

- [45] The CTA Consortium. Design concepts for the cherenkov telescope array. *arXiv preprint arXiv:1008.3703*, 2010.
- [46] Hamish Silverwood, Christoph Weniger, Pat Scott, and Gianfranco Bertone. A realistic assessment of the cta sensitivity to dark matter annihilation. *Journal of Cosmology and Astroparticle Physics*, 2015(03):055, 2015.
- [47] The Cherenkov Telescope Array Consortium, BS Acharya, I Agudo, I Al Samarai, R Alfaro, J Alfaro, C Alispach, R Alves Batista, J-P Amans, E Amato, et al. Science with the cherenkov telescope array. *arXiv preprint arXiv:1709.07997*, 2017.
- [48] O Adriani, Y Akaike, K Asano, Y Asaoka, MG Bagliesi, G Bigongiari, WR Binns, S Bonechi, M Bongi, JH Buckley, et al. The calorimetric electron telescope (calet) for high-energy astroparticle physics on the international space station. *Journal of Physics: Conference Series*, 632(1):012023, 2015.
- [49] NP Topchiev, AM Galper, V Bonvicini, O Adriani, RL Aptekar, IV Arkhangel'skaja, AI Arkhangel'skiy, AV Bakaldin, L Bergstrom, E Berti, et al. Gamma-400 gamma-ray observatory. *arXiv preprint arXiv:1507.06246*, 2015.
- [50] Xiaoyuan Huang, Anna S Lamperstorfer, Yue-Lin Sming Tsai, Ming Xu, Qiang Yuan, Jin Chang, Yong-Wei Dong, Bing-Liang Hu, Jun-Guang Lü, Le Wang, et al. Perspective of monochromatic gamma-ray line detection with the high energy cosmic-radiation detection (herd) facility onboard china's space station. *Astroparticle Physics*, 78:35–42, 2016.
- [51] Silvia Galli, Fabio Iocco, Gianfranco Bertone, and Alessandro Melchiorri. Cmb constraints on dark matter models with large annihilation cross section. *Physical Review D*, 80(2):023505, 2009.
- [52] Antony Lewis, Jochen Weller, and Richard Battye. The cosmic microwave background and the ionization history of the universe. *Monthly Notices of the Royal Astronomical Society*, 373(2):561–570, 2006.
- [53] Silvia Galli, Rachel Bean, Alessandro Melchiorri, and Joseph Silk. Delayed recombination and cosmic parameters. *Phys. Rev. D*, 78:063532, Sep 2008.
- [54] Jaiseung Kim and Pavel Naselsky. Accelerated recombination, and the acbar and wmap data. *The Astrophysical Journal Letters*, 678(1):L1, 2008.
- [55] N Aghanim, M Arnaud, M Ashdown, J Aumont, C Baccigalupi, AJ Banday, RB Barreiro, JG Bartlett, N Bartolo, E Battaner, et al. Planck 2015 results-xi. cmb power spectra, likelihoods, and robustness of parameters. *Astronomy & Astrophysics*, 594:A11, 2016.
- [56] Le Zhang, Xuelei Chen, Yi-An Lei, and Zong-guo Si. Impacts of dark matter particle annihilation on recombination and the anisotropies of the cosmic microwave background. *Physical Review D*, 74(10):103519, 2006.
- [57] A Lewis, A Challinor, and A Lasenby. Efficient computation of cmb anisotropies in closed frw models. *Astrophys. J*, 538:473, 2000.
- [58] Sara Seager, Dimitar D Sasselov, and Douglas Scott. How exactly did the universe become neutral? *The Astrophysical Journal Supplement Series*, 128(2):407, 2000.
- [59] PJE Peebles. Recombination of the primeval plasma. *The Astrophysical Journal*, 153:1, 1968.
- [60] Nikhil Padmanabhan and Douglas P Finkbeiner. Detecting dark matter annihilation with cmb polarization: Signatures and experimental prospects. *Physical Review D*, 72(2):023508, 2005.

- [61] O Adriani, GC Barbarino, GA Bazilevskaia, R Bellotti, M Boezio, EA Bogomolov, L Bonechi, M Bongi, V Bonvicini, S Bottai, et al. Observation of an anomalous positron abundance in the cosmic radiation. *arXiv preprint arXiv:0810.4995*, 2008.
- [62] Ilias Cholis, Douglas P Finkbeiner, Lisa Goodenough, and Neal Weiner. The pamel positron excess from annihilations into a light boson. *Journal of Cosmology and Astroparticle Physics*, 2009(12):007, 2009.
- [63] Massimiliano Lattanzi and Joseph Silk. Can the wimp annihilation boost factor be boosted by the sommerfeld enhancement? *Physical Review D*, 79(8):083523, 2009.
- [64] Jesus Zavala, Mark Vogelsberger, and Simon DM White. Relic density and cmb constraints on dark matter annihilation with sommerfeld enhancement. *Physical Review D*, 81(8):083502, 2010.
- [65] Tracy R. Slatyer. Indirect dark matter signatures in the cosmic dark ages. I. Generalizing the bound on s-wave dark matter annihilation from Planck results. *Physical Review D*, 93(2):023527, jan 2016.
- [66] Mathew S. Madhavacheril, Neelima Sehgal, and Tracy R. Slatyer. Current dark matter annihilation constraints from CMB and low-redshift data. *Physical Review D*, 89(10):103508, may 2014.
- [67] Sara Seager, Dimitar D. Sasselov, and Douglas Scott. RECFast: Calculate the Recombination History of the Universe. *Astrophysics Source Code Library, record ascl:1106.026*, 2011.
- [68] G. Hütsi, J. Chluba, A. Hektor, and M. Raidal. WMAP7 and future CMB constraints on annihilating dark matter: implications for GeV-scale WIMPs. *Astronomy & Astrophysics*, 535:A26, nov 2011.
- [69] D Larson, J Dunkley, G Hinshaw, Eiichiro Komatsu, MR Nolte, CL Bennett, B Gold, M Halpern, RS Hill, N Jarosik, et al. Seven-year wilkinson microwave anisotropy probe (wmap*) observations: power spectra and wmap-derived parameters. *The Astrophysical Journal Supplement Series*, 192(2):16, 2011.
- [70] DJ Eisenstein et al. Detection of the baryon acoustic peak in the large-scale correlation function of sdss luminous red galaxies. *Astrophys. J*, 633:560, 2005.
- [71] Laura Lopez-Honorez, Olga Mena, Sergio Palomares-Ruiz, and Aaron C Vincent. Constraints on dark matter annihilation from CMB observations before Planck. *Journal of Cosmology and Astroparticle Physics*, 2013(07):046–046, jul 2013.
- [72] E. Komatsu, J. Dunkley, M. R. Nolte, C. L. Bennett, B. Gold, G. Hinshaw, N. Jarosik, D. Larson, M. Limon, L. Page, D. N. Spergel, M. Halpern, R. S. Hill, A. Kogut, S. S. Meyer, G. S. Tucker, J. L. Weiland, E. Wollack, and E. L. Wright. Five-Year Wilkinson Microwave Anisotropy Probe Observations: Cosmological Interpretation. *The astrophysical journal*, 180:330–376, February 2009.
- [73] NASA. <https://wmap.gsfc.nasa.gov/>. *NASA webpage*, 2001.
- [74] Peter AR Ade, N Aghanim, M Arnaud, M Ashdown, J Aumont, C Baccigalupi, AJ Banday, RB Barreiro, JG Bartlett, N Bartolo, et al. Planck 2015 results-xiii. cosmological parameters. *Astronomy & Astrophysics*, 594:A13, 2016.
- [75] Pasquale Dario Serpico and Pasquale D. Possible causes of a rise with energy of the cosmic ray positron fraction. *Physical Review D*, vol. 79, Issue 2, id. 021302, 79(2), oct 2008.

- [76] Pasquale D. Serpico. Astrophysical models for the origin of the positron “excess”. *Astroparticle Physics*, 39-40:2–11, dec 2012.
- [77] Oscar Adriani, GC Barbarino, GA Bazilevskaya, R Bellotti, Mirko Boezio, EA Bogomolov, L Bonechi, M Bongi, Valter Bonvicini, S Bottai, et al. An anomalous positron abundance in cosmic rays with energies 1.5–100 gev. *Nature*, 458(7238):607, 2009.
- [78] O Adriani, GC Barbarino, GA Bazilevskaya, R Bellotti, M Boezio, EA Bogomolov, L Bonechi, M Bongi, V Bonvicini, S Borisov, et al. A statistical procedure for the identification of positrons in the pamelas experiment. *Astroparticle Physics*, 34(1):1–11, 2010.
- [79] Giuseppe Di Bernardo, Carmelo Evoli, Daniele Gaggero, Dario Grasso, and Luca Maccione. Unified interpretation of cosmic ray nuclei and antiproton recent measurements. *Astroparticle Physics*, 34(5):274–283, dec 2010.
- [80] J. Lavalle. Impact of the spectral hardening of TeV cosmic rays on the prediction of the secondary positron flux. *Monthly Notices of the Royal Astronomical Society*, 414(2):985–991, jun 2011.
- [81] Boaz Katz, Kfir Blum, Jonathan Morag, and Eli Waxman. What can we really learn from positron flux ‘anomalies’? jul 2009.
- [82] I. V. Moskalenko and A. W. Strong. Production and Propagation of Cosmic-Ray Positrons and Electrons. *The Astrophysical Journal*, 493(2):694–707, feb 1998.
- [83] Qiang Yuan and Xiao-Jun Bi. Reconcile the AMS-02 positron fraction and Fermi-LAT/HESS total e^\pm spectra by the primary electron spectrum hardening. *Physics Letters B*, 727(1-3):1–7, nov 2013.
- [84] Nir J. Shaviv, Ehud Nakar, and Tsvi Piran. Inhomogeneity in the Supernova Remnant Distribution as the Origin of the PAMELA Anomaly. *Physical Review Letters*, 103(11):111302, feb 2009.
- [85] James Stockton. Average inhomogeneities in Milky Way SNII and the PAMELA anomaly. *Astroparticle Physics*, 35(3):161–163, oct 2011.
- [86] Markus Ackermann, Marco Ajello, A Allafort, WB Atwood, Luca Baldini, Guido Barbiellini, D Bastieri, K Bechtol, R Bellazzini, B Berenji, et al. Measurement of separate cosmic-ray electron and positron spectra with the fermi large area telescope. *Physical Review Letters*, 108(1):011103, 2012.
- [87] Dan Hooper, Albert Stebbins, and Kathryn M. Zurek. Excesses in cosmic ray positron and electron spectra from a nearby clump of neutralino dark matter. *Physical Review D*, 79(10):103513, may 2009.
- [88] Wan-Lei Guo and Yue-Liang Wu. Enhancement of Dark Matter Annihilation via Breit-Wigner Resonance. jan 2009.
- [89] Stuart L. Shapiro and Saul A. Teukolsky. Black holes, white dwarfs, and neutron stars: The physics of compact objects. *Research supported by the National Science Foundation. New York, Wiley-Interscience, 1983, 663 p.*, 1983.
- [90] Roland Diehl, Hubert Halloin, Karsten Kretschmer, Gisela G. Lichti, Volker Schoenfelder, Andrew W. Strong, Andreas von Kienlin, Wei Wang, Pierre Jean, Juergen Knoedlseder, Jean-Pierre Roques, Georg Weidenspointner, Stephane Schanne, Dieter H. Hartmann, Christoph Winkler, and Cornelia Wunderer. Radioactive ^{26}Al and massive stars in the Galaxy. jan 2006.

- [91] S.-H. Lee, T. Kamae, L. Baldini, F. Giordano, M.-H. Grondin, L. Latronico, M. Lemoine-Goumard, C. Sgrò, T. Tanaka, and Y. Uchiyama. Explaining the cosmic-ray $e^+/(e^- + e^+)$ and p^-/p ratios using a steady-state injection model. *Astroparticle Physics*, 35(4):211–222, nov 2011.
- [92] L. Zhang and K. S. Cheng. Cosmic-ray positrons from mature gamma-ray pulsars. *Astronomy & Astrophysics*, 368(3):1063–1070, mar 2001.
- [93] S. W. Barwick, J. J. Beatty, A. Bhattacharyya, C. R. Bower, C. J. Chaput, S. Coutu, G. A. de Nolfo, J. Knapp, D. M. Lowder, S. McKee, D. Müller, J. A. Musser, S. L. Nutter, E. Schneider, S. P. Swordy, G. Tarlé, A. D. Tomasch, E. Torbet, and The Heat Collaboration. Measurements of the Cosmic-Ray Positron Fraction from 1 to 50 G[CLC]e/[CLC]V. *The Astrophysical Journal*, 482(2):L191–L194, jun 1997.
- [94] Georg G. Raffelt. Supernova neutrino observations: What can we learn? *Nuclear Physics B - Proceedings Supplements*, 221:218–229, dec 2011.
- [95] John Ellis, RA Flores, Katherine Freese, S Ritz, D Seckel, and Joseph Silk. Cosmic ray constraints on the annihilations of relic particles in the galactic halo. *Physics Letters B*, 214(3):403–412, 1988.
- [96] Pasquale D Serpico. Astrophysical models for the origin of the positron “excess”. *Astroparticle Physics*, 39:2–11, 2012.
- [97] F Donato, D Maurin, P Brun, T Delahaye, and P Salati. Constraints on wimp dark matter from the high energy pamea p/p data. *Physical review letters*, 102(7):071301, 2009.
- [98] M Aguilar, L Ali Cavasonza, B Alpat, G Ambrosi, L Arruda, N Attig, S Aupetit, P Azzarello, A Bachlechner, F Barao, et al. Antiproton flux, antiproton-to-proton flux ratio, and properties of elementary particle fluxes in primary cosmic rays measured with the alpha magnetic spectrometer on the international space station. *Physical review letters*, 117(9):091103, 2016.
- [99] O Adriani, GC Barbarino, GA Bazilevskaya, R Bellotti, M Boezio, EA Bogomolov, L Bonechi, M Bongi, V Bonvicini, S Borisov, et al. Pamela measurements of cosmic-ray proton and helium spectra. *arXiv preprint arXiv:1103.4055*, 2011.
- [100] Mathieu Boudaud, Marco Cirelli, Gaëlle Giesen, and Pierre Salati. A fussy revisitation of antiprotons as a tool for dark matter searches. *Journal of Cosmology and Astroparticle Physics*, 2015(05):013, 2015.
- [101] Mattia Di Mauro, Fiorenza Donato, Andreas Goudelis, and Pasquale Dario Serpico. New evaluation of the antiproton production cross section for cosmic ray studies. *Physical Review D*, 90(8):085017, 2014.
- [102] Gaëlle Giesen, Mathieu Boudaud, Yoann Genolini, Vivian Poulin, Marco Cirelli, Pierre Salati, and Pasquale D Serpico. Ams-02 antiprotons, at last! secondary astrophysical component and immediate implications for dark matter. *Journal of Cosmology and Astroparticle Physics*, 2015(09):023, 2015.
- [103] Marco Cirelli, Daniele Gaggero, Gaëlle Giesen, Marco Taoso, and Alfredo Urbano. Antiproton constraints on the gev gamma-ray excess: a comprehensive analysis. *Journal of Cosmology and Astroparticle Physics*, 2014(12):045, 2014.
- [104] Marco Cirelli, Gennaro Corcella, Andi Hektor, Gert Hütsi, Mario Kadastik, Paolo Panci, Martti Raidal, Filippo Sala, and Alessandro Strumia. Pppc 4 dm id: a poor particle physicist cookbook for dark matter indirect detection. *Journal of Cosmology and Astroparticle Physics*, 2011(03):051, 2011.

- [105] Paolo Ciafaloni, Marco Cirelli, Denis Comelli, Andrea De Simone, Antonio Riotto, and Alfredo Urbano. On the importance of electroweak corrections for majorana dark matter indirect detection. *Journal of Cosmology and Astroparticle Physics*, 2011(06):018, 2011.
- [106] Nicole F Bell, James B Dent, Thomas D Jacques, and Thomas J Weiler. Dark matter annihilation signatures from electroweak bremsstrahlung. *Physical Review D*, 84(10):103517, 2011.
- [107] R. Duperray, B. Baret, D. Maurin, G. Boudoul, A. Barrau, L. Derome, K. Protasov, and M. Buénerd. Flux of light antimatter nuclei near Earth, induced by cosmic rays in the Galaxy and in the atmosphere. *Physical Review*, 71(8):083013, April 2005.
- [108] F. Donato, N. Fornengo, and P. Salati. Antideuterons as a signature of supersymmetric dark matter. *Physical Review*, 62(4):043003, August 2000.
- [109] N. Fornengo, L. Maccione, and A. Vittino. Dark matter searches with cosmic antideuterons: status and perspectives. *Journal of Cosmology and Astroparticle Physics*, 9:031, September 2013.
- [110] M. Cirelli, N. Fornengo, M. Taoso, and A. Vittino. Anti-helium from dark matter annihilations. *Journal of High Energy Physics*, 8:9, August 2014.
- [111] F. Donato, N. Fornengo, D. Maurin, P. Salati, and R. Taillet. Antiprotons in cosmic rays from neutralino annihilation. *Physical Review*, 69(6):063501, March 2004.
- [112] Jan Conrad and Olaf Reimer. Indirect dark matter searches in gamma and cosmic rays. *Nature Physics*, 13(3):224, 2017.
- [113] Silvia Adrián-Martínez, A Albert, Michel André, G Anton, M Ardid, J-J Aubert, T Avgitas, B Baret, J Barrios-Martí, S Basa, et al. Limits on dark matter annihilation in the sun using the antares neutrino telescope. *Physics letters B*, 759:69–74, 2016.
- [114] MG Aartsen, K Abraham, M Ackermann, Joe Adams, JA Aguilar, M Ahlers, M Ahrens, D Altmann, K Andeen, T Anderson, et al. All-flavour search for neutrinos from dark matter annihilations in the milky way with icecube/deepcore. *The European Physical Journal C*, 76(10):531, 2016.
- [115] Chris Gordon and Oscar Macias. Dark matter and pulsar model constraints from galactic center fermi-lat gamma-ray observations. *Physical Review D*, 88(8):083521, 2013.
- [116] Francesca Calore, Ilias Cholis, and Christoph Weniger. Background model systematics for the fermi gev excess. *Journal of Cosmology and Astroparticle Physics*, 2015(03):038, 2015.
- [117] NW Evans, JL Sanders, and Alex Geringer-Sameth. Simple j-factors and d-factors for indirect dark matter detection. *Physical Review D*, 93(10):103512, 2016.
- [118] A Albert, Michel André, Marco Anghinolfi, G Anton, M Ardid, J-J Aubert, T Avgitas, B Baret, J Barrios-Martí, S Basa, et al. Results from the search for dark matter in the milky way with 9 years of data of the antares neutrino telescope. *Physics letters B*, 769:249–254, 2017.
- [119] Alex Geringer-Sameth, Savvas M Koushiappas, and Matthew Walker. Dwarf galaxy annihilation and decay emission profiles for dark matter experiments. *The Astrophysical Journal*, 801(2):74, 2015.
- [120] Andreas Burkert. The structure of dark matter halos in dwarf galaxies. *The Astrophysical Journal Letters*, 447(1):L25, 1995.